

1 **Marine terraces of the last interglacial period along the Pacific** 2 **coast of South America (1°N-40°S)**

3 Roland Freisleben¹, Julius Jara-Muñoz¹, Daniel Melnick^{2,3}, José Miguel Martínez^{2,3}, Manfred R.
4 Strecker¹

5 ¹ Institut für Geowissenschaften, Universität Potsdam, 14476 Potsdam, Germany

6 ² Instituto de Ciencias de la Tierra, TAQUACH, Universidad Austral de Chile, Valdivia, Chile

7 ³ Millennium Nucleus The Seismic Cycle Along Subduction Zones, Valdivia, Chile

8 *Correspondence to:* Roland Freisleben (freisleb@uni-potsdam.de)

9 **Abstract.** Tectonically active coasts are dynamic environments characterized by the presence of multiple marine
10 terraces formed by the combined effects of wave-erosion, tectonic uplift, and sea-level oscillations at glacial-cycle
11 timescales. Well-preserved erosional terraces from the last interglacial sea-level highstand are ideal marker horizons
12 for reconstructing past sea-level positions and calculating vertical displacement rates. We carried out an almost
13 continuous mapping of the last interglacial marine terrace along ~5,000 km of the western coast of South America
14 between 1°N and 40°S. We used quantitatively replicable approaches constrained by published terrace-age estimates
15 to ultimately compare elevations and patterns of uplifted terraces with tectonic and climatic parameters in order to
16 evaluate the controlling mechanisms for the formation and preservation of marine terraces, and crustal deformation.
17 Uncertainties were estimated on the basis of measurement errors and the distance from referencing points. Overall,
18 our results indicate a median elevation of 30.1 m, which would imply a median uplift rate of 0.22 m/ka averaged over
19 the past ~125 ka. The patterns of terrace elevation and uplift rate display high-amplitude (~100–200 m) and long-
20 wavelength (~10² km) structures at the Manta Peninsula (Ecuador), the San Juan de Marcona area (central Peru), and
21 the Arauco Peninsula (south-central Chile). Medium-wavelength structures occur at the Mejillones Peninsula and
22 Topocalma in Chile, while short-wavelength (< 10 km) features are for instance located near Los Vilos, Valparaíso,
23 and Carranza, Chile. We interpret the long-wavelength deformation to be controlled by deep-seated processes at the
24 plate interface such as the subduction of major bathymetric anomalies like the Nazca and Carnegie ridges. In contrast,
25 short-wavelength deformation may be primarily controlled by sources in the upper plate such as crustal faulting,
26 which, however, may also be associated with the subduction of topographically less pronounced bathymetric
27 anomalies. Latitudinal differences in climate additionally control the formation and preservation of marine terraces.
28 Based on our synopsis we propose that increasing wave height and tidal range result in enhanced erosion and
29 morphologically well-defined marine terraces in south-central Chile. Our study emphasizes the importance of using
30 systematic measurements and uniform, quantitative methodologies to characterize and correctly interpret marine
31 terraces at regional scales, especially if they are used to unravel tectonic and climatic forcing mechanisms of their
32 formation. This database is an integral part of the World Atlas of Last Interglacial Shorelines (WALIS), published
33 online at <http://doi.org/10.5281/zenodo.4309748> (Freisleben et al., 2020).

34 **1. Introduction**

35 Tectonically active coasts are highly dynamic geomorphic environments and they host densely-populated centers and
36 associated infrastructure (Melet et al., 2020). Coastal areas have been episodically affected by the effects of sea-level
37 changes at glacial timescales, modifying the landscape and leaving behind fossil geomorphic markers, such as former
38 paleo-shorelines, and marine terraces (Lajoie, 1986). One of the most prominent coastal landforms are marine terraces
39 that were generated during the protracted last interglacial sea-level highstand that occurred ~125 ka ago (Siddall et
40 al., 2006; Hearty et al., 2007; Pedroja et al., 2011). These terraces are characterized by a higher preservation potential,
41 which facilitates their recognition, mapping, and lateral correlation. Furthermore, because of their high degree of
42 preservation and relatively young age, they have been used to estimate vertical deformation rates at local and regional
43 scales. The relative abundance and geomorphic characteristics of the last interglacial marine terraces make them ideal
44 geomorphic markers with which to reconstruct past sea-level positions and to enable comparisons between distant
45 sites under different climatic and tectonic settings.

46 The Western South American Coast (WSAC) is a tectonically active region that has been repeatedly affected by
47 megathrust earthquakes and associated surface deformation (Beck et al., 1998; Melnick et al., 2006; Bilek, 2010;
48 Baker et al., 2013). Interestingly, previous studies have shown that despite the broad spectrum of latitudinal climatic
49 conditions and erosional regimes along the WSAC, marine terraces are scattered, but omnipresent along the coast (Ota
50 et al., 1995; Regard et al., 2010; Rehak et al., 2010; Bernhardt et al., 2016; Melnick, 2016; Bernhardt et al., 2017).
51 However, only a few studies on interglacial marine terraces have been conducted along the WSAC, primarily in
52 specific areas where they are best expressed; this has resulted in disparate and inconclusive marine terrace
53 measurements based on different methodological approaches and ambiguous interpretations concerning their origin
54 in a tectonic and climatic context (Hsu et al., 1989; Ortlieb and Macharé, 1990; Hsu, 1992; Macharé and Ortlieb, 1992;
55 Pedroja et al., 2006b; Saillard et al., 2009; Pedroja et al., 2011; Saillard et al., 2011; Rodríguez et al., 2013). This lack
56 of reliable data points has revealed a need to re-examine the last interglacial marine terraces along the WSAC based
57 on standardized methodologies in order to obtain a systematic and continuous record of marine terrace elevations
58 along the coast. This information is crucial in order to increase our knowledge of the climatic and tectonic forcing
59 mechanisms that contributed to the formation and degradation of marine terraces in this region.

60 Marine terrace sequences at tectonically active coasts are landforms formed by wave erosion and/or accumulation of
61 sediments resulting from the interaction between tectonic uplift and superposed oscillating sea-level changes (Lajoie,
62 1986; Anderson et al., 1999; Jara-Muñoz et al., 2015). Typically, marine terrace elevations are estimated based on the
63 shoreline angle. The marine terrace morphology comprises a gently inclined erosional or depositional paleo-platform
64 that terminates landward at a steeply sloping paleo-cliff surface. The intersection point between both surfaces
65 represents the approximate sea-level position during the formation of the marine terrace also known as shoreline angle;
66 if coastal uplift is rapid, such uplifting abrasion or depositional surfaces may be preserved in the landscape and remain
67 unaltered by the effects of subsequent sea-level oscillations (Lajoie, 1986).

68 The analysis of elevation patterns based on shoreline-angle measurements at subduction margins has been largely used
69 to estimate vertical deformation rates and the mechanisms controlling deformation, including the interaction of the
70 upper plate with bathymetric anomalies, the activity of crustal faults in the upper plate, and deep-seated processes
71 such as basal accretion of subducted trench sediments (Taylor et al., 1987; Hsu, 1992; Macharé and Ortlieb, 1992; Ota
72 et al., 1995; Pedoja et al., 2011; Saillard et al., 2011; Jara-Muñoz et al., 2015; Melnick, 2016). The shoreline angle
73 represents a 1D descriptor of the marine terrace elevation, whose measurements are reproducible when using
74 quantitative morphometric approaches (Jara-Muñoz et al., 2016). Furthermore, the estimation of the marine terrace
75 elevations based on shoreline angles can be further improved by quantifying their relationship with paleo-sea level,
76 also known as the indicative meaning (Lorscheid and Rovere, 2019).

77 In this continental-scale compilation of marine terrace elevations along the WSAC, we present systematically mapped
78 shoreline angles of marine terraces of the last (Eem/Sangamon) interglacial obtained along 5,000 km of coastline
79 between 1°N and 40°S. In this synthesis we rely on chronological constraints from previous regional studies and
80 compilations (Pedoja et al., 2011). For the first time we are able to introduce an almost continuous pattern of terrace
81 elevation and coastal uplift rates at a spatial scale of 10^3 km along the WSAC. Furthermore, in our database we
82 compare tectonic and climatic parameters to elucidate the mechanisms controlling the formation and preservation of
83 marine terraces, and patterns of crustal deformation along the coast. This study was thus primarily intended to provide
84 a comprehensive, standardized database and description of last interglacial marine terrace elevations along the
85 tectonically active coast of South America. This database therefore affords future research into coastal environments
86 to decipher potential tectonic forcings with regard to the deformation and seismotectonic segmentation of the forearc;
87 as such this database will ultimately help to decipher the relationship between upper-plate deformation, vertical motion
88 and bathymetric anomalies and aid in the identification of regional fault motions along pre-existing anisotropies in the
89 South American continental plate. Finally, our database includes information on climate-driving forcing mechanisms
90 that may influence the formation, modification and/or destruction of marine terraces in different climatic sectors along
91 the South American convergent margin. This new database is part of the World Atlas of Last Interglacial Shorelines
92 (WALIS), published online at <http://doi.org/10.5281/zenodo.4309748> (Freisleben et al., 2020).

93 **2. Geologic and geomorphic setting of the WSAC**

94 **2.1. Tectonic and seismotectonic setting**

95 **2.1.1. Subduction geometry and bathymetric features**

96 The tectonic setting of the convergent margin of South America is controlled by subduction of the oceanic Nazca plate
97 beneath the South American continental plate. The convergence rate varies between 66 mm/a in the north (8°S latitude)
98 and 74 mm/a in the south (27°S latitude) (Fig. 1). The convergence azimuth changes slightly from N81.7° toward
99 N77.5° from north to south (DeMets et al., 2010). The South American subduction zone is divided into four major
100 segments with variable subduction angles inferred from the spatial distribution of Benioff seismicity (Barazangi and
101 Isacks, 1976; Jordan et al., 1983) (Fig. 1). The segments beneath northern and central Peru (2°–15°S) and beneath

102 central Chile (27°–33°S) are characterized by a gentle dip of the subducting plate between 5° and 10° at depths of
103 ~100 km (Hayes et al., 2018), whereas the segments beneath southern Peru and northern Chile (15°–27°S), and beneath
104 southern Chile (33°–45°S) have steeper dips of 25° to 30°. Spatial distributions of earthquakes furthermore indicate a
105 steep-slab subduction segment in Ecuador and southern Colombia (2°S to 5°N), and a flat-slab segment in NW
106 Colombia (north of 5°N) (Pilger, 1981; Cahill and Isacks, 1992; Gutscher et al., 2000; Ramos and Folguera, 2009).
107 Processes that have been inferred to be responsible for the shallowing of the subduction slab include the subduction
108 of large buoyant ridges or plateaus (Espurt et al., 2008) as well as the combination of trenchward motion of thick,
109 buoyant continental lithosphere accompanied by trench retreat (Sobolev and Babeyko, 2005; Manea et al., 2012).
110 Volcanic activity as well as the forearc architecture and distribution of upper-plate deformation further emphasize the
111 location of flat-slab subduction segments (Jordan et al., 1983; Kay et al., 1987; Ramos and Folguera, 2009).

112 Several high bathymetric features have been recognized on the subducting Nazca plate. The two most prominent
113 bathymetric features being subducted beneath South America are the Carnegie and Nazca aseismic ridges at 0° and
114 15°S, respectively; they consist of seamounts related to hot-spot volcanism (e.g., Gutscher et al., 1999; Hampel, 2002).
115 The 300-km-wide and ~2-km-high Carnegie Ridge subducts roughly parallel with the convergence direction and its
116 geometry should have remained relatively stable beneath the continental plate (Angermann et al., 1999; Gutscher et
117 al., 1999; DeMets et al., 2010; Martinod et al., 2016a). In contrast, the obliquity of the 200-km-wide and 1.5-km-high
118 Nazca Ridge with respect to the convergence direction resulted in 500 km SE-directed migration of its locus of ridge
119 subduction during the last 10 Ma (Hampel, 2002; Saillard et al., 2011; Martinod et al., 2016a). Similarly, smaller
120 aseismic ridges such as the Juan Fernández Ridge and the Iquique Ridge subduct beneath the South American
121 continent at 32°S and 21°S, respectively. The intercepts between these bathymetric anomalies and the upper plate are
122 thought to influence the characteristics of interplate coupling and seismic rupture (Bilek et al., 2003; Wang and Bilek,
123 2011; Geersen et al., 2015; Collot et al., 2017) and mark the boundaries between flat and steep subduction segments
124 and changes between subduction erosion and accretion (Jordan et al., 1983; von Huene et al., 1997; Ramos and
125 Folguera, 2009) (Fig. 1).

126 In addition to bathymetric anomalies, several studies have shown that variations in the volume of sediments in the
127 trench may control the subduction regime from an erosional mode to an accretionary mode (von Huene and Scholl,
128 1991; Bangs and Cande, 1997). In addition, the volume of sediment in the trench has also been hypothesized to
129 influence the style of interplate seismicity (Lamb and Davis, 2003). At the southern Chile margin, thick trench-
130 sediment sequences and a steeper subduction angle correlate primarily with subduction accretion, although the area
131 of the intercept of the continental plate with the Chile Rise spreading center locally exhibits the opposite case (von
132 Huene and Scholl, 1991; Bangs and Cande, 1997). Subduction erosion characterizes the region north of the southern
133 volcanic zone from central and northern Chile to southern Peru (33°–15°S) due to decreasing sediment supply to the
134 trench, especially within the flat-slab subduction segments (Stern, 1991; von Huene and Scholl, 1991; Bangs and
135 Cande, 1997; Clift and Vannucchi, 2004). Clift and Hartley (2007) and Lohrmann et al. (2003) argued for an alternate
136 style of slow tectonic erosion leading to underplating of subducted material below the base of the crustal forearc,
137 synchronous with tectonic erosion beneath the trenchward part of the forearc. For the northern Andes, several authors

138 also classify the subduction zone as an erosional type (Clift and Vannucchi, 2004; Scholl and Huene, 2007; Marcaillou
139 et al., 2016).

140 2.1.2. Major continental fault systems in the coastal realm

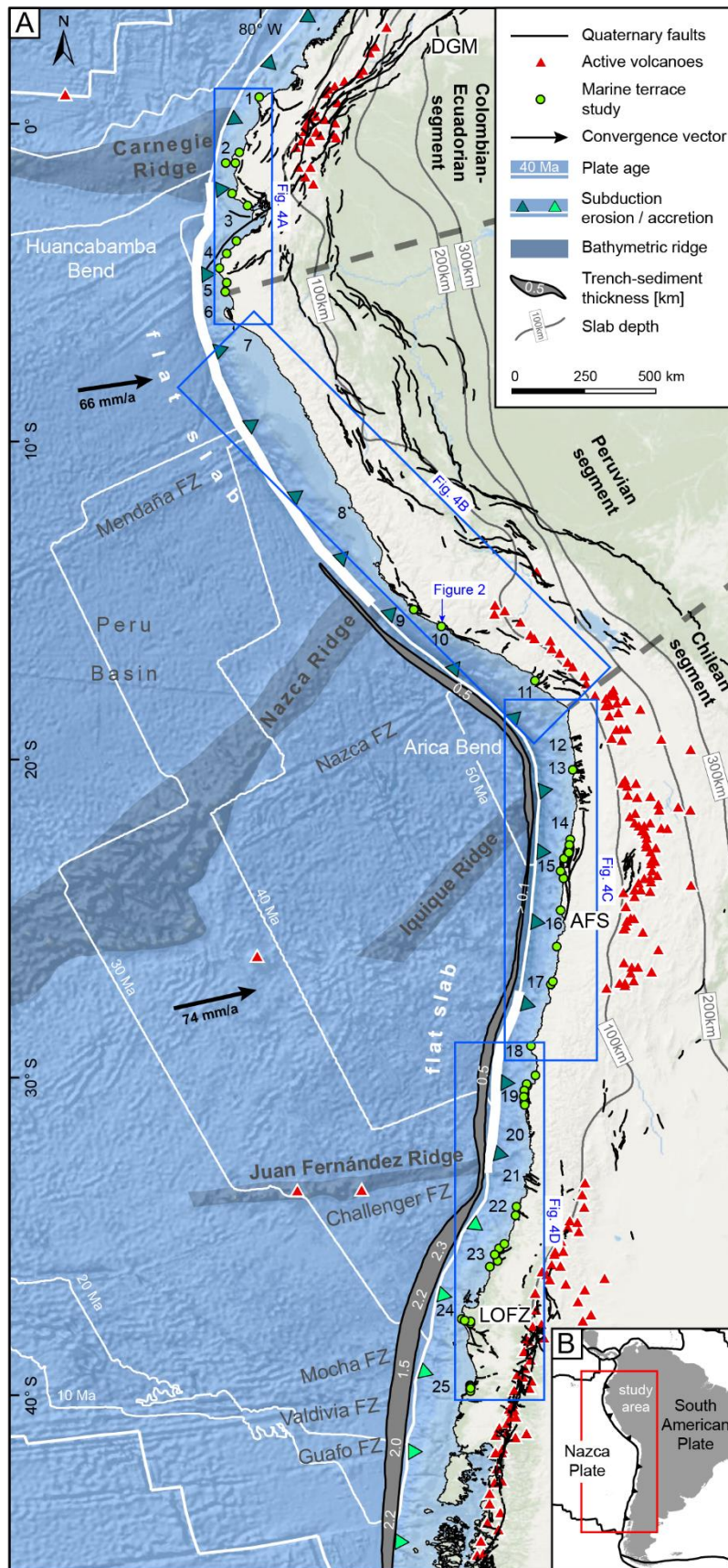
141 The South American convergent margin comprises several fault systems with different kinematics, whose presence is
142 closely linked to oblique subduction and the motion and deformation of forearc slivers. Here we summarize the main
143 structures that affect the Pacific coastal areas. North of the Talara bend (5°S), active thrusting and dextral strike-slip
144 faulting dominates the coastal lowlands of Ecuador (e.g., Mache, Bahía, Jipijapa faults), although normal faulting also
145 occurs at Punta Galera (Cumilínche fault) and the Manta Peninsula (Río Salado fault) (Fig. 1). Farther south, normal
146 faulting is active in the Gulf of Guayaquil (Posorja fault) and dextral strike-slip faulting occurs at the Santa Elena
147 Peninsula (La Cruz fault) (Veloza et al., 2012; Costa et al., 2020). The most prominent dextral fault in this region is
148 the 2000-km-long, northeast-striking Dolores-Guayaquil megashear (DGM), which starts in the Gulf of Guayaquil
149 and terminates in the Colombian hinterland east of the range-bounding thrust faults of the Colombian Andes (Veloza
150 et al., 2012; Villegas-Lanza et al., 2016; Costa et al., 2020) (Fig. 1). Normal faults have been described along the coast
151 of Peru at the Illescas Peninsula in the north (6°S) in the San Juan de Marcona area with the El Huevo-Lomas fault
152 system (14.5°–16°S), and the Incapuquio fault system in the south (17°–18°S) (Veloza et al., 2012; Villegas-Lanza et
153 al., 2016; Costa et al., 2020). The main fault zones of the Chilean convergent margin comprise the Atacama Fault
154 System (AFS) in the Coastal Cordillera extending from Iquique to La Serena (29.75°S, Fig. 1), with predominantly
155 N-S-striking normal faults, which result in relative uplift of their western side (e.g., Mejillones fault, Salar del Carmen
156 fault) (Naranjo, 1987; González and Carrizo, 2003; Cembrano et al., 2007). Coastal fault systems farther south are
157 located in the Altos de Talinay area (30.5°S, Puerto Aldea fault), near Valparaíso (33°S, Quintay and Valparaíso
158 faults), near the Arauco Peninsula (36°–39°S, Santa María and Lanalhue faults), and in between these areas
159 (Topocalma, Pichilemu, Carranza, and Pelluhue faults) (Ota et al., 1995; Melnick et al., 2009; Santibáñez et al., 2019;
160 Melnick et al., 2020; Maldonado et al., 2021) (Fig. 1). However, there is still limited knowledge regarding Quaternary
161 slip rates and kinematics and, most importantly, the location of active faults along the forearc region of South America
162 (Jara-Muñoz et al., 2018; Melnick et al., 2019).

163 2.2. Climate and geomorphic setting

164 2.2.1. Geomorphology

165 The 8000-km-long Andean orogen is a major, hemisphere-scale feature that can be divided into ~~different~~ segments
166 with distinctive geomorphic and tectonic characteristics. The principal segments comprise the NNE-SSW trending
167 Colombian-Ecuadorian segment (12°N–5°S), the NW-SE oriented Peruvian segment (5°–18°S), and the N-S trending
168 Chilean segment (18°–56°S) (Jaillard et al., 2000) (Fig. 1). Two major breaks separate these segments; these are the
169 Huancabamba bend in northern Peru and the Arica bend at the Peru-Chile border. The distance of the trench from the
170 WSAC coastline averages 118 km and ranges between 44 and 217 km. The depth of the trench ~~fluctuates~~ between

varies



172 2920 and 8177 m (GEBCO Bathymetric Compilation Group, 2020), and the continental shelf has an average width of
173 28 km (Paris et al., 2016).

174 In the 50- to 180-km-wide coastal area of the Ecuadorian Andes, where the Western Cordillera is flanked by a
175 structural depression, relief is relatively low (< 300 m asl). The Gulf of Guayaquil (3°S) and the Dolores-Guayaquil
176 megashear separate the northern from the southern forearc units. The coast-trench distance along the Huancabamba
177 bend is quite small (~55–90 km), except for the Gulf of Guayaquil, and the trench east of the Carnegie Ridge is at a
178 relatively shallow depth of ~3.5 km. Farther south, the Peruvian forearc comprises the up to 160-km-wide Coastal
179 Plains in the north and the narrow, 3000-m-high Western Cordillera. While the Coastal Plains in north-central Peru
180 are relatively narrow (< 40 km), they widen in southern Peru, and the elevation of the Western Cordillera increases to
181 more than 5000 m (Suárez et al., 1983; Jaillard et al., 2000). The region between the coast and the trench in central
182 Peru (up to 220 km) narrows toward the San Juan de Marcona area (~75 km) near the intercept with the Nazca Ridge,
183 and the relatively deep trench (~6.5 km) becomes shallower (< 5 km) (GEBCO Bathymetric Compilation Group,
184 2020). Between 18°S and 28°S, the Chilean forearc comprises the 50-km-wide and up to 2700-m-high Coastal
185 Cordillera, which is separated from the Precordillera by the Central Depression. In the flat-slab subduction segment
186 between 27°S and 33°S there is neither a morphotectonic region characterized by a central depression nor active
187 volcanism in the high Andean cordillera (Fig. 1) (Jordan et al., 1983). The Chilean forearc comprises the Coastal
188 Cordillera, which varies in altitude from up to 2000 m at 33°S to 500 m at 46°S, and the Central Depression that
189 separates the forearc from the Main Cordillera. From the Arica bend, where the coast-trench distance is up to 170 km
190 and the trench ~8 km deep, a slight increase in coast-trench distance can be observed in Chile toward the south (~80–
191 130 km), as can a decrease in trench depth to ~4.5 km.

192 2.2.2. Marine terraces and coastal uplift rates

193 Wave erosion forms wave-cut terrace levels, while the accumulation of shallow marine sediments during sea-level
194 highstands forms wave-built terraces. Another type of terrace is known as “rasa” and refers to wide shore platforms
195 formed under slow-uplift conditions (< 0.2 m/ka), and the repeated reoccupation of this surface by high sea levels
196 (Regard et al., 2010; Rodríguez et al., 2013; Melnick, 2016). Other studies indicate a stronger influence of climate and
197 rock resistance to erosion compared to marine wave action (Prémaillon et al., 2018). Typically, the formation of
198 Pleistocene marine terraces in the study area occurred during interglacial and interstadial relative sea-level highstands
199 that were superposed on the uplifting coastal areas; according to the Quaternary oxygen-isotope curve defining warm
200 and cold periods, high Quaternary sea levels have been correlated with warm periods and are denoted with the odd-
201 numbered Marine Isotope Stages (MIS) (Lajoie, 1986; Shackleton et al., 2003).

202 Along the WSAC, staircase-like sequences of multiple marine terraces are preserved nearly continuously along the
203 coast. These terraces comprise primarily wave-cut surfaces that are frequently covered by beach ridges of siliciclastic
204 sediments and local accumulations of carbonate bioclastic materials associated with beach ridges (Ota et al., 1995;
205 Saillard et al., 2009; Rodríguez et al., 2013; Martinod et al., 2016b). Rasa surfaces exist in the regions of southern
206 Peru and northern Chile (Regard et al., 2010; Rodríguez et al., 2013; Melnick, 2016). Particularly the well-preserved

207 MIS-5e terrace level has been largely used as a strain marker in the correlation of uplifted coastal sectors due to its
208 lateral continuity and high potential for preservation. Global observations of sea-level fluctuations during MIS-5 allow
209 to differentiate between three second-order highstands at 80 ka (5a), 105 ka (5c), and 128 to 116 ka (5e) with paleo-
210 sea levels of -20 m for both of the younger and $+3 \pm 3$ m for the oldest highstand (Stirling et al., 1998; Siddall et al.,
211 2006; Hearty et al., 2007; Rohling et al., 2009; Pedoja et al., 2011). The database generated in this study is based
212 exclusively in the last interglacial marine terraces exposed along the WSAC, between Ecuador and Southern Chile
213 (1°S to 40°S). In the following section we present a brief review of previously studied marine terrace sites in this area.

214 Paleo-shoreline elevations of the last interglacial (MIS-5e) in Ecuador are found at elevations of around 45 ± 2 m asl
215 in Punta Galera (Esmeraldas area), $43\text{--}57 \pm 2$ m on the Manta Peninsula and La Plata Island, and 15 ± 5 m asl on the
216 Santa Elena Peninsula (Pedoja et al., 2006b; Pedoja et al., 2006a). In northern Peru, MIS-5e terraces have been
217 described at elevations of 18–31 m asl for the Tablazo Lobitos (Cancas and Mancora areas), at 25 ± 5 m asl on the
218 Paita Peninsula, and at 18 ± 3 m asl on the Illescas Peninsula and the Bay of Bayovar (Pedoja et al., 2006b). Farther
219 south, MIS-5e terraces are exceptionally high in the San Juan de Marcona area immediately south of the subducting
220 Nazca Ridge, with maximum elevations of 80 m at the Cerro Tres Hermanas and 105 m at the Cerro El Huevo (Hsu
221 et al., 1989; Ortlieb and Macharé, 1990; Saillard et al., 2011). The Pampa del Palo region in southern Peru exhibits
222 relatively thick vertical stacks of shallow marine terrace deposits related to MIS-7, 5e (~20 m), and 5c that may
223 indicate a different geodynamic behavior compared to adjacent regions (Ortlieb et al., 1996b). In central and northern
224 Chile, the terrace levels of the last interglacial occur at 250–400 m, 150–240 m, 80–130 m, and 30–40 m, and in
225 southern Chile at 170–200 m, 70 m, 20–38 m, 8–10 m (Fuenzalida et al., 1965). Specifically, between 24°S and 32°S ,
226 paleo-shoreline elevations of the last interglacial (MIS-5e) range between 25 and 45 m (Ota et al., 1995; Saillard et
227 al., 2009; Martinod et al., 2016b). Shore platforms are higher in the Altos de Talinay area ($30.3^{\circ}\text{--}31.3^{\circ}\text{S}$), but are
228 small, poorly preserved, and terminate at a high coastal scarp between 26.75°S and 24°S (Martinod et al., 2016b).
229 Shoreline-angle elevations between 34° and 38°S (along the Maule seismotectonic segment) vary from high altitudes
230 in the Arauco and Topocalma areas (200 m) to moderate elevations near Caranza (110 m), and very low elevations in
231 between (15 m) (Melnick et al., 2009; Jara-Muñoz et al., 2015).

232 Coastal uplift-rate estimates along the WSAC mainly comprise calculations for the Talara Arc, the San Juan de
233 Marcona area, the Mejillones Peninsula, the Altos de Talinay area, and several regions in south-central Chile. Along
234 the Talara Arc (6.5°S to 1°N), marine terraces of the Manta Peninsula and La Plata Island in central Ecuador indicate
235 the most pronounced uplift rates of 0.31 to 0.42 m/ka since MIS-5e, while similar uplift rates are documented to the
236 north in the Esmeraldas area (0.34 m/ka), and lower ones to the south at the Santa Elena Peninsula (0.1 m/ka). In
237 northern Peru, last interglacial uplift rates are relative low, ranging from 0.17–0.21 m/ka for the Tablazo Lobitos and
238 0.16 m/ka for the Paita Peninsula, to 0.12 m/ka for the Bay of Bayovar and the Illescas Peninsula (Pedoja et al., 2006b;
239 Pedoja et al., 2006a). Marine terraces on the continental plate above the subducting Nazca Ridge ($13.5^{\circ}\text{--}15.6^{\circ}\text{S}$) record
240 variations in uplift rate where the coastal forearc above the northern flank of the ridge is either stable or has undergone
241 net subsidence (Macharé and Ortlieb, 1992). The coast above the ridge crest is rising at about 0.3 m/ka and the coast
242 above the southern flank (San Juan de Marcona) is uplifting at a rate of 0.5 m/ka (Hsu, 1992) or even 0.7 m/ka (Ortlieb

→ although
GSA
can
cause
local
differences
of up to
30 m
depending
on
location
(González
et al.,
2017;
Simón
et al.,
2016)

243 and Macharé, 1990) for at least the last 125 ka. Saillard et al. (2011) state that long-term regional uplift in the San
244 Juan de Marcona area has increased since about 800 ka related to the southward migration of the Nazca Ridge, and
245 ranges from 0.44 to 0.87 m/ka. The Pampa del Palo area in southern Peru rose more slowly or was even down-faulted
246 and had subsided with respect to the adjacent coastal regions (Ortlieb et al., 1996b). These movements ceased after
247 the highstand during the MIS-5e and slow uplift rates of approximately 0.16 m/ka have characterized the region since
248 100 ka (Ortlieb et al., 1996b). In northern Chile (24°–32°S), uplift rates for the Late Pleistocene average around 0.28
249 ± 0.15 m/ka (Martinod et al., 2016b), except for the Altos de Talinay area, where pulses of rapid uplift occurred during
250 the Middle Pleistocene (Ota et al., 1995; Saillard et al., 2009; Martinod et al., 2016b). The Central Andean *rasa* (15°–
251 33°S) and Lower to Middle Pleistocene shore platforms – which are also generally wider – indicate a period of tectonic
252 stability or subsidence followed by accelerated and spatially continuous uplift after ~400 ka (MIS-11) (Regard et al.,
253 2010; Rodríguez et al., 2013; Martinod et al., 2016b). However, according to Melnick (2016), the Central Andean *rasa*
254 has experienced slow and steady long-term uplift with a rate of 0.13 ± 0.04 m/ka during the Quaternary, predominantly
255 accumulating strain through deep earthquakes at the crust-mantle boundary (Moho) below the locked portion of the
256 plate interface. The lowest uplift rates occur at the Arica bend and increase gradually southward; the highest values
257 are attained along geomorphically distinct peninsulas (Melnick, 2016). In the Maule segment (34°–38°S), the mean
258 uplift rate for the MIS-5 terrace level is 0.5 m/ka, exceeded only in the areas of Topocalma, Carranza, and Arauco,
259 where it amounts to 1.6 m/ka (Melnick et al., 2009; Jara-Muñoz et al., 2015). Although there are several studies of
260 marine terraces along the WSAC, these are isolated and based on different methodological approaches, mapping and
261 leveling resolution, as well as dating techniques, which makes regional comparisons and correlations difficult in the
262 context of the data presented here.

263 **2.2.3. Climate**

264 Apart from latitudinal temperature changes, the present-day morphotectonic provinces along the South American
265 margin have a pronounced impact on the precipitation gradients on the west coast of South America. Since mountain
266 ranges are oriented approximately perpendicular to moisture-bearing winds, they affect both flanks of the orogen
267 (Strecker et al., 2007). The regional-scale pattern of wind circulation is dominated by westerly winds at
268 subtropical/extratropical latitudes primarily up to about 27°S (Garreaud, 2009). However, anticyclones over the South
269 Pacific result in winds blowing from the south along the coast between 35°S and 10°S (Garreaud, 2009). The moisture
270 in the equatorial Andes (Ecuador and Colombia) and in the areas farther south (27°S) is fed by winds from the Amazon
271 basin and the Gulf of Panama, resulting in rainfall mainly on the eastern flanks of the mountain range (Bendix et al.,
272 2006; Bookhagen and Strecker, 2008; Garreaud, 2009). The Andes of southern Ecuador, Peru, and northern Chile are
273 dominated by a rain-shadow effect that causes aridity within the Andean Plateau (Altiplano-Puna), the Western
274 Cordillera, and the coastal region (Houston and Hartley, 2003; Strecker et al., 2007; Garreaud, 2009). Furthermore,
275 the aridity is exacerbated by the effects of the cold Humboldt current, which prevents humidity from the Pacific from
276 penetrating inland (Houston and Hartley, 2003; Garreaud, 2009; Coudurier-Curveur et al., 2015). The precipitation
277 gradient reverses between 27°S and 35°S, where the Southern Hemisphere Westerlies cause abundant rainfall on the
278 western flanks of the Coastal and Main cordilleras (Garreaud, 2009). Martinod et al. (2016b) proposed that latitudinal

279 differences in climate largely influence coastal morphology, specifically the formation of high coastal scarps that
280 prevent the development of extensive marine terrace sequences. However, the details of this relationship have not
281 been conclusively studied along the full extent of the Pacific coast of South America.

282 3. Methods

283 We combined – and describe in detail below – bibliographic information, different topographic data sets, and uniform
284 morphometric and statistical approaches to assess the elevation of marine terraces and accompanying vertical
285 deformation rates along the western South American margin.

286 3.1. Mapping marine terraces

287 Marine terraces are primarily described based on their elevation, which is essential for determining vertical
288 deformation rates. The measurements of the marine terrace elevations of the last interglacial were performed using
289 TanDEM-X topography (12 and 30 m horizontal resolution) (German Aerospace Center (DLR), 2018), and digital
290 terrain models from LiDAR (1, 2.5, and 5 m horizontal resolution). The DEMs were converted to orthometric heights
291 by subtracting the EGM2008 geoid and projected in UTM using the World Geodetic System (WGS1984) using zone
292 19S for Chile, zone 18S for southern/central Peru, and zone 17S for northern Peru/Ecuador.

293 To trace the MIS-5 shoreline, we mapped its inner edge along the west coast of South America based on slope changes
294 on TanDEM-X topography at the foot of paleo-cliffs (Jara-Muñoz et al., 2016) (Fig. 2A and B). To facilitate mapping,
295 we used slope and hillshade maps. We correlated the results of the inner-edge mapping with the marine terraces catalog
296 of Pedoja et al. (2011) and references therein (section 2.2.2, Table 1). Further references used to validate MIS-5e
297 terrace heights include Victor et al. (2011) for the Pampa de Mejillones, Martinod et al. (2016b) for northern Chile,
298 and Jara-Muñoz et al. (2015) for the area between 34° and 38°S. We define the term “referencing point” for these
299 previously published terrace heights and age constraints. The referencing point with the shortest distance to the
300 location of our measurements served as a topographical and chronological benchmark for mapping the MIS-5 terrace
301 in the respective areas. In addition, this distance is used to assign a quality rating to our measurements.

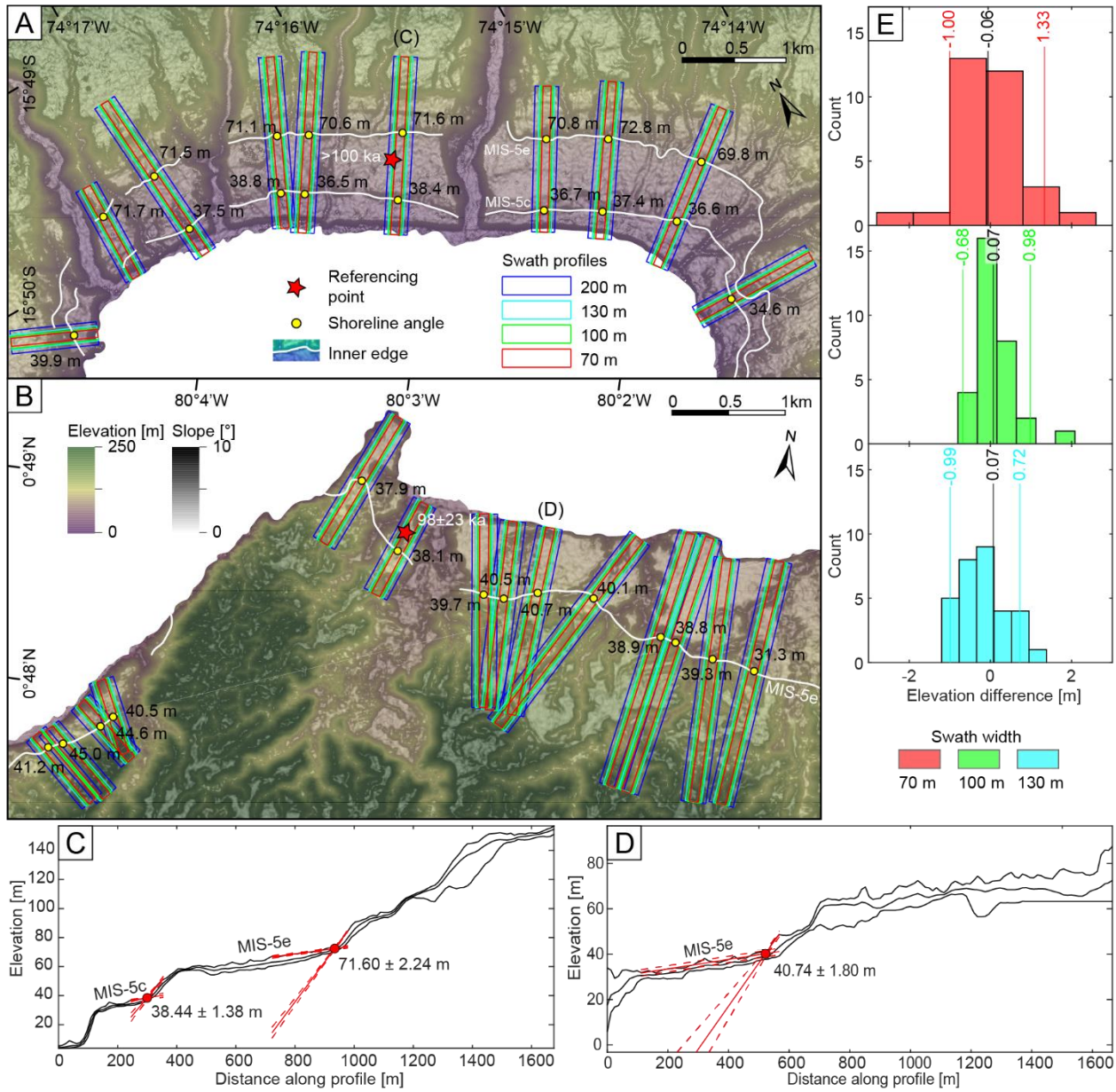
302 In addition to MIS-5e, we also mapped MIS-5c in areas with high uplift rates such as at the Manta Peninsula, San
303 Juan de Marcona, Topocalma, Carranza, and Arauco. Although we observed a terrace level correlated to MIS-5a in
304 the Marcona area, we excluded this level from the database due to its limited preservation at other locations and lack
305 of chronological constraints. Our assignment of mapped terrace levels to MIS-5c is primarily based on age constraints
306 by Saillard et al. (2011) for the Marcona area and Jara-Muñoz et al. (2015) for the area between 34° and 38°S.
307 However, in order to evaluate the possibility that our correlation with MIS-5c is flawed, we estimated uplift rates for
308 the lower terraces by assigning them tentatively to either MIS-5a or MIS-5c. We interpolated the uplift rates derived
309 from the MIS-5e level at the sites of the lower terraces and compared the differences (Figure 3A). If we infer that
310 uplift rates were constant in time at each site throughout the three MIS-5 substages, the comparison suggests these
311 lower terrace levels correspond to MIS-5c because of the smaller difference in uplift rate, rather than to MIS-5a (Figure
312 3B).

→ same as shoreline angle?
what elevations were you using for MIS-5c?

313 A rigorous assessment of marine terrace elevations is crucial for determining accurate vertical deformation rates. Since
314 fluvial degradation and hillslope processes after the abandonment of marine terraces may alter their morphology
315 (Anderson et al., 1999; Jara-Muñoz et al., 2015), direct measurements of terrace elevations at the inner edge (foot of
316 the paleo-cliff) may result in overestimation of the terrace elevations and vertical deformation rates (Jara-Muñoz et
317 al., 2015). To precisely measure the shoreline-angle elevations of the MIS-5 terrace level, we used a profile-based
318 approach in TerraceM, a graphical user interface in MATLAB® (Jara-Muñoz et al., 2016), available at
319 www.terracem.com. We placed swath profiles of variable width perpendicular to the previously mapped inner edge,
320 which were used by the TerraceM algorithm to extract maximum elevations to avoid fluvial incision (Fig. 2A and B).
321 For the placement of the swath profiles we tried to capture a local representation of marine terrace topography with a
322 sufficiently long, planar paleo-platform, and a sufficiently high paleo-cliff, simultaneously avoiding topographic
323 disturbance, such as colluvial wedges or areas characterized by river incision. North of Caleta Chañaral (29°S), we
324 used swath profiles of 200 m width, although we occasionally used 100-m-wide profiles for narrow terrace remnants.
325 South of 29°S, we used swath widths of 130 and 70 m. The width was chosen based on fluvial drainage densities ~~that~~
326 are associated with climate gradients. Sensitivity tests comparing shoreline-angle measurements from different swath
327 widths in the Chala Bay and at Punta Galera show only minimal vertical deviations of less than 0.5 m (Fig. 2E). The
328 sections of these profiles, which represent the undisturbed paleo-platform and paleo-cliff, were picked manually and
329 fitted by linear regression. The extrapolated intersection between both regression lines ultimately determines the
330 buried shoreline-angle elevation and associated uncertainty, which is derived from the 95% confidence interval (2σ)
331 of both regressions (Fig. 2C and D). In total, we measured 1843 MIS-5e and 110 MIS-5c shoreline-angle elevations.
332 To quantify the paleo-position of the relative sea-level elevation and the involved uncertainty for the WALIS template,
333 we calculated the indicative meaning using the IMCalc software from Lorscheid and Rovere (2019). The indicative
334 meaning comprises the range between the lower and upper limits of sea-level formation – the indicative range – as
335 well as its mathematically averaged position, which corresponds to the reference water level (Lorscheid and Rovere,
336 2019).

earlier
when
1st
mentioning
inner
edge

at which
locations?
a couple representative
locations?



337

338 **Figure 2. Orthometrically corrected TanDEM-X and slope map of (A) Chala Bay in south-central Peru and (B) Punta**
 339 **Punta Galera in northern Ecuador with mapped inner shoreline edges of the MIS-5e and 5c terrace levels. Colored rectangles**
 340 **represent swath-profile boxes of various widths that were placed perpendicular to the inner edges for the subsequent**
 341 **estimation of terrace elevation in TerraceM. The red star indicates the referencing point with the age constraint for the**
 342 **respective area (Pedoja et al., 2006b; Saillard, 2008). (C) and (D) Estimation of the shoreline-angle elevation in TerraceM**
 343 **by intersecting linear-regression fits of the paleo-cliff and paleo-platform (200-m-wide swath profiles). (E) Histograms of**
 344 **elevation differences measured in both areas for various swath widths (70 m, 100 m, and 130 m) with respect to the 200-m-**
 345 **wide reference swath profile (blue). Vertical lines indicate median values and standard deviations (2σ).**

346

347

348

349

350 **Table 1. Age constraints used for mapping of the inner edge of MIS-5 and for verifying our terrace-elevation measurements.**
351 **This compilation is mainly based on the terrace catalog of Pedoja et al. (2011); added references include Victor et al. (2011)**
352 **for Pampa de Mejillones, Martinod et al. (2016b) for northern Chile, and Jara-Muñoz et al. (2015) for south-central Chile.**
353 **Absolute ages refer to MIS-5e marine terraces, unless otherwise specified; inferred ages refer to their associated MIS. IRSL:**
354 **Infrared Stimulated Luminescence, AAR: Amino-Acid Racemization, CRN: Cosmogenic Radionuclides, ESR: Electron**
355 **Spin Resonance.**

Country	Location	Lat.	Long.	Dating method	Confidence	Reference	Age [ka]
Ecuador	Galera	0.81	-80.03	IRSL	5	Pedoja et al., 2006b	98±23
Ecuador	Manta	-0.93	-80.66	IRSL, U/Th	5	Pedoja et al., 2006b	76±18, 85±1
Ecuador	La Plata	-1.26	-81.07	U/Th	5	Pedoja et al., 2006b	104±2
Ecuador	Manta	-1.27	-80.78	IRSL	5	Pedoja et al., 2006b	115±23
Ecuador	Santa Elena	-2.21	-80.88	U/Th	5	Pedoja et al., 2006b	136±4, 112±2
Ecuador	Puna	-2.60	-80.40	U/Th	5	Pedoja et al., 2006b	98±3, 95±0
Peru	Cancas	-3.72	-80.75	Morphostratigraphy	5	Pedoja et al., 2006b	~125
Peru	Mancora/ Lobitos	-4.10	-81.05	Morphostratigraphy	5	Pedoja et al., 2006b	~125
Peru	Talara	-4.56	-81.28	Morphostratigraphy	5	Pedoja et al., 2006b	~125
Peru	Paita	-5.03	-81.06	Morphostratigraphy	5	Pedoja et al., 2006b	~125
Peru	Bayovar/ Illescas	-5.31	-81.10	IRSL	5	Pedoja et al., 2006b	111±6
Peru	Cerro Huevo	-15.31	-75.17	CRN	5	Saillard et al., 2011	228±28 (7e)
Peru	Chala Bay	-15.85	-74.31	CRN	5	Saillard, 2008	> 100
Peru	Ilo	-17.55	-71.37	AAR	5	Ortlieb et al., 1996b; Hsu et al., 1989	~125, ~105
Chile	Punta Lobos	-20.35	-70.18	U/Th, ESR	5	Radtke, 1989	~125
Chile	Cobija	-22.55	-70.26	Morphostratigraphy	4	Ortlieb et al., 1995	~125, ~105
Chile	Michilla	-22.71	-70.28	AAR	3	Leonard & Wehmiller, 1991	~125
Chile	Hornitos	-22.85	-70.30	U/Th	5	Ortlieb et al., 1996a	108±1, 118±6
Chile	Chacaya	-22.95	-70.30	AAR	5	Ortlieb et al., 1996a	~125
Chile	Pampa Mejillones	-23.14	-70.45	U/Th	5	Victor et al., 2011	124±3
Chile	Mejillones/ Punta Jorge	-23.54	-70.55	U/Th, ESR	3	Radtke, 1989	~125
Chile	Coloso	-23.76	-70.46	ESR	3	Schellmann & Radtke, 1997	106±3
Chile	Punta Piedras	-24.76	-70.55	CRN	5	Martinod et al., 2016b	138±15
Chile	Esmeralda	-25.91	-70.67	CRN	5	Martinod et al., 2016b	79±9
Chile	Caldera	-27.01	-70.81	U/Th, ESR	5	Marquardt et al., 2004	~125
Chile	Bahia Inglesa	-27.10	-70.85	U/Th, ESR	5	Marquardt et al., 2004	~125
Chile	Caleta Chanaral	-29.03	-71.49	CRN	5	Martinod et al., 2016b	138±0
Chile	Coquimbo	-29.96	-71.34	AAR	5	Leonard & Wehmiller, 1992; Hsu et al., 1989	~125
Chile	Punta Lengua de Vaca	-30.24	-71.63	U/Th	5	Saillard et al., 2012	95±2 (5c)
Chile	Punta Lengua de Vaca	-30.30	-71.61	U/Th	5	Saillard et al., 2012	386±124 (11)
Chile	Quebrada Palo Cortado	-30.44	-71.69	CRN	5	Saillard et al., 2009	149±10

Chile	Rio Limari	-30.63	-71.71	CRN	5	Saillard et al., 2009	318±30 (9c)
Chile	Quebrada de la Mula	-30.79	-71.70	CRN	5	Saillard et al., 2009	225±17 (7e)
Chile	Quebrada del Teniente	-30.89	-71.68	CRN	5	Saillard et al., 2009	678±51 (17)
Chile	Puertecillo	-34.09	-71.94	IRSL	5	Jara-Munoz et al., 2015	87±7 (5c)
Chile	Pichilemu	-34.38	-71.97	IRSL	5	Jara-Munoz et al., 2015	106±9 (5c)
Chile	Putu	-35.16	-72.25	IRSL	5	Jara-Munoz et al., 2015	85±8 (5c)
Chile	Constitucion	-35.40	-72.49	IRSL	5	Jara-Munoz et al., 2015	105±8 (5c)
Chile	Constitucion	-35.44	-72.47	IRSL	5	Jara-Munoz et al., 2015	124±11
Chile	Carranza	-35.58	-72.61	IRSL	5	Jara-Munoz et al., 2015	67±6 (5c)
Chile	Carranza	-35.64	-72.54	IRSL	5	Jara-Munoz et al., 2015	104±9
Chile	Pelluhue	-35.80	-72.54	IRSL	5	Jara-Munoz et al., 2015	112±10
Chile	Pelluhue	-35.80	-72.55	IRSL	5	Jara-Munoz et al., 2015	102±9 (5c)
Chile	Curanipe	-35.97	-72.78	IRSL	5	Jara-Munoz et al., 2015	265±29
Chile	Arauco	-37.62	-73.67	IRSL	5	Jara-Munoz et al., 2015	89±9 (5c)
Chile	Arauco	-37.68	-73.57	CRN	5	Melnick et al., 2009	127±13
Chile	Arauco	-37.71	-73.39	CRN	5	Melnick et al., 2009	133±14
Chile	Arauco	-37.76	-73.38	CRN	5	Melnick et al., 2009	130±13
Chile	Cerro Caleta Curiñanco	-39.72	-73.40	Tephrochronology	4	Pino et al., 2002	~125
Chile	South Curiñanco	-39.76	-73.39	Tephrochronology	4	Pino et al., 2002	~125
Chile	Valdivia	-39.80	-73.39	Tephrochronology	4	Pino et al., 2002	~125
Chile	Camping Bellavista	-39.85	-73.40	Tephrochronology	4	Pino et al., 2002	~125
Chile	Mancera	-39.89	-73.39	Tephrochronology	5	Silva, 2005	~125

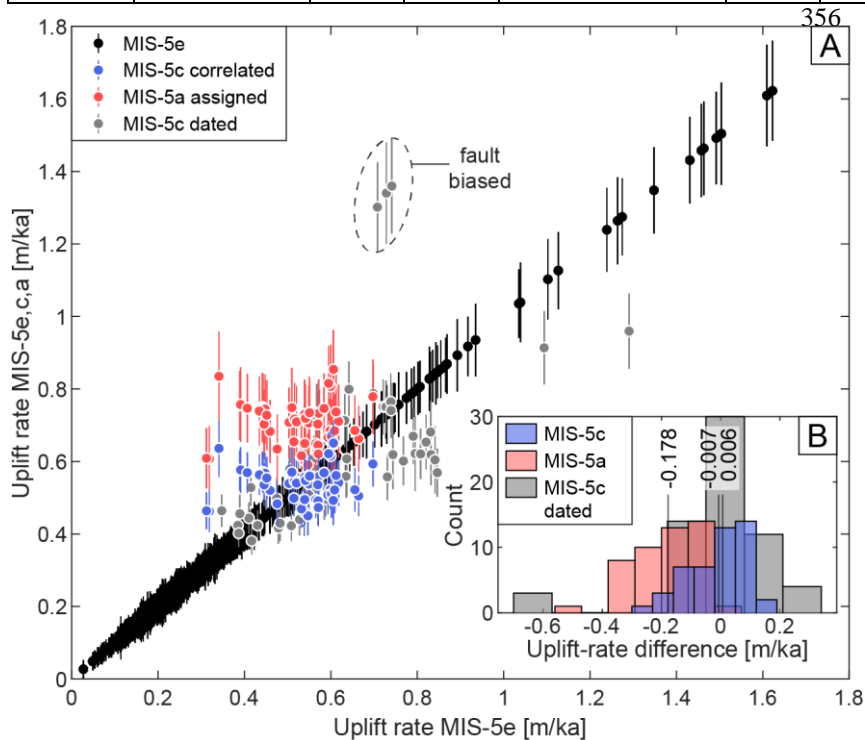


Figure 3. Comparison of MIS-5 uplift-rate estimates. (A) Uplift rates derived by correlating mapped terrace occurrences located immediately below the MIS-5e level to either MIS-5c (blue) or MIS-5a (red) with respect to MIS-5e uplift rates. Marine terraces correlated to MIS-5c by an age constraint are plotted in gray color. (B) Histograms of differences between MIS-5a or MIS-5c uplift rates and MIS-5e uplift rates. Vertical lines show median uplift-rate differences.

what elevations did you use for MIS 5a & 5c

375 To quantify the reliability and consistency of our shoreline-angle measurements, we developed a quality rating from
376 low (1) to high (5) confidence. Equation 1 illustrates how we calculated the individual parameters and the overall
377 quality rating:

378 **Equation 1: Quality rating.**

$$379 \quad QR = 1 + 2.4 * \left(\frac{C_{RP}}{\max(C_{RP})} * \left(1 - \frac{D_{RP}}{\max(D_{RP})} \right) \right)^e + 1.2 * \left(1 - \frac{E_T}{\max(E_T)} \right) + 0.4 * 1.2 * \left(1 - \frac{R}{\max(R)} \right)$$

380 The four parameters ~~that we~~ included in our quality rating (QR) comprise a) the distance to the nearest referencing
381 point (D_{RP}), b) the confidence of the referencing point ~~that is~~ based on the dating method used by previous studies
382 (C_{RP}) (Pedoja et al., 2011), c) the measurement error in TerraceM (E_T), and (d) the pixel-scale resolution of the
383 topographic data set (R) (Fig. 4). We did not include the error that results from the usage of different swath widths,
384 since the calculated elevation difference with respect to the most frequently used 200 m swath width is very low (<
385 0.5 m) (Fig. 2E). From the reference points we only used data points with a confidence value of 3 or greater (1 – poor,
386 5 – very good) based on the previous qualification of Pedoja et al. (2011). The confidence depends mainly on the
387 reliability of the dating method, but can be increased by good age constraints of adjacent terrace levels or detailed
388 morphostratigraphic correlations, such as in Chala Bay (Fig. 2A) (Goy et al., 1992; Saillard, 2008). We further used
389 this confidence value to quantify the quality of the age constraints in the WALIS template.

390 To account for the different uncertainties of the individual parameters in the QR, we combined and weighted the
391 parameters D_{RP} and C_{RP} in a first equation claiming 60% of the final QR, E_T in a second and R in a third equation
392 weighted 30% and 10%, respectively. We justify these percentages by the fact that the distance and confidence to the
393 nearest referencing point is of utmost importance for identifying the MIS-5e terrace level. The measurement error
394 represents how well the mapping of the paleo-platform and paleo-cliff resulted in the shoreline-angle measurement,
395 while the topographic resolution of the underlying DEM only influences the precise representation of the actual
396 topography and has little impact on the measurement itself. The coefficient assigned to the topographic resolution is
397 multiplied by a factor of 1.2 in order to maintain the possibility of a maximum QR for a DEM resolution of 5 m.
398 Furthermore, we added an exponent to the first part of the equation to reinforce low confidence and/or high distance
399 of the referencing point for low quality ratings. The exponent adjusts the QR according to the distribution of distances
400 from referencing points, which follows an exponential relationship (Fig. 4D).

401 The influence of each parameter to the quality rating can be observed in Fig. 4. We observe that for high D_{RP} values
402 the QR becomes constant; likewise, the influence of QR parameters becomes significant for QR values higher than 3.
403 We justify the constancy of the QR for high D_{RP} values (> 300 km) by the fact that most terrace measurements have
404 D_{RP} values below 200 km (Fig. 4D). The quality rating is then used as a descriptor of the confidence of marine terrace-
405 elevation measurements.

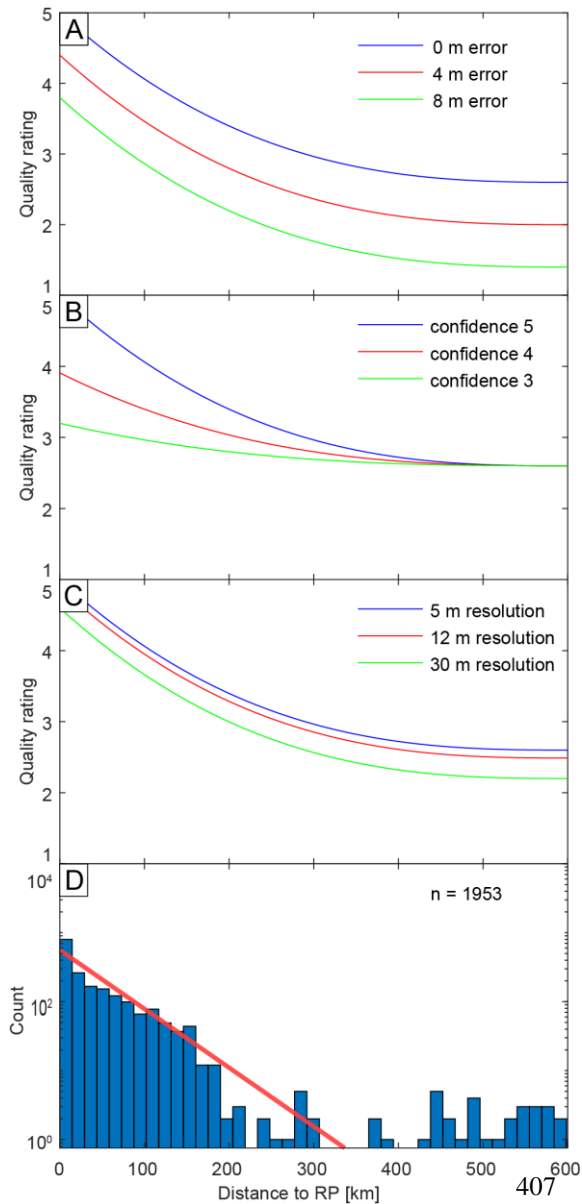


Figure 4. Influence of the parameters on the quality rating. The x-axis is the distance to reference point (RP), the y-axis is the quality rating, the color lines represent different values of quality rating parameters. While one parameter is being tested, the remaining parameters are set to their best values. That is why the QR does not reach values of 1 in the graphs displayed here. (A) Shoreline-angle elevation error. (B) Confidence value of the referencing point. (C) Topographic resolution of the DEM used for terrace-elevation estimation. (D) Histogram displaying the distribution of distances between each shoreline-angle measurement and its nearest RP (n: number of measurements). The red line is an exponential fit.

408 3.2. Estimating coastal uplift rates

409 Uplift-rate estimates from marine terraces (u) were calculated using equations 2 and 3:

410 **Equation 2: Relative sea level.**

$$411 \quad \Delta H = H_T - H_{SL}$$

412 **Equation 3: Uplift rate.**

$$413 \quad u = \frac{H_T - H_{SL}}{T}$$

414 where ΔH is the relative sea level, H_{SL} is the sea-level altitude of the interglacial maximum, H_T is the shoreline-angle
415 elevation of the marine terrace, and T its associated age (Lajoie, 1986).

416 We calculated the standard error $SE(u)$ using equation 4 from Gallen et al. (2014):

417 **Equation 4: Uplift-rate error.**

418
$$SE(u)^2 = u^2 \left(\left(\frac{\sigma_{\Delta H}^2}{\Delta H^2} \right) + \left(\frac{\sigma_T^2}{T^2} \right) \right)$$

419 where $\sigma_{\Delta H}^2$, the error in relative sea level, equals $(\sigma_{H_T}^2 + \sigma_{H_{SL}}^2)$. The standard-error estimates comprise the uncertainty
420 in shoreline-angle elevations from TerraceM (σ_{H_T}), error estimates in absolute sea level ($\sigma_{H_{SL}}$) from Rohling et al.
421 (2009), and an arbitrary range of 10 ka for the duration of the highstand (σ_T).

422 Vertical displacement rates and relative sea level are influenced by flexural rebound associated with loading and
423 unloading of ice sheets during glacio-isostatic adjustments (GIA) (Stewart et al., 2000; Shepherd and Wingham, 2007).
424 The amplitude and wavelength of GIA is mostly determined by the flexural rigidity of the lithosphere (Turcotte and
425 Schubert, 1982) and should therefore not severely influence vertical deformation along non-glaciated coastal regions
426 (Rabassa and Clapperton, 1990) that are located in the forearc of active subduction zones. Because of their intrinsic
427 modeling complexities, we did not account for the GIA effect on terrace elevations and uplift rates.

but
vary
locally
and
across
the
region
due to
GIA

more
acknowledgment

428 **3.3 Tectonic parameters of the South American convergent margin**

also
visually
response

429 We compared the deformation patterns of marine terraces along the coast of South America with proxies that included
430 crustal faults, bathymetric anomalies, trench-sediment thickness, and distance to the trench. To evaluate the possible
431 control of climatic parameters in the morphology of marine terraces, we compared our data set with wave heights,
432 tidal range, mean annual precipitation rate, and the azimuth of the coastline (Schweller et al., 1981; Bangs and Cande,
433 1997; von Huene et al., 1997; Collot et al., 2002; Ceccherini et al., 2015; Hayes et al., 2018; Santibáñez et al., 2019;
434 GEBCO Bathymetric Compilation Group, 2020) (Fig. 1).

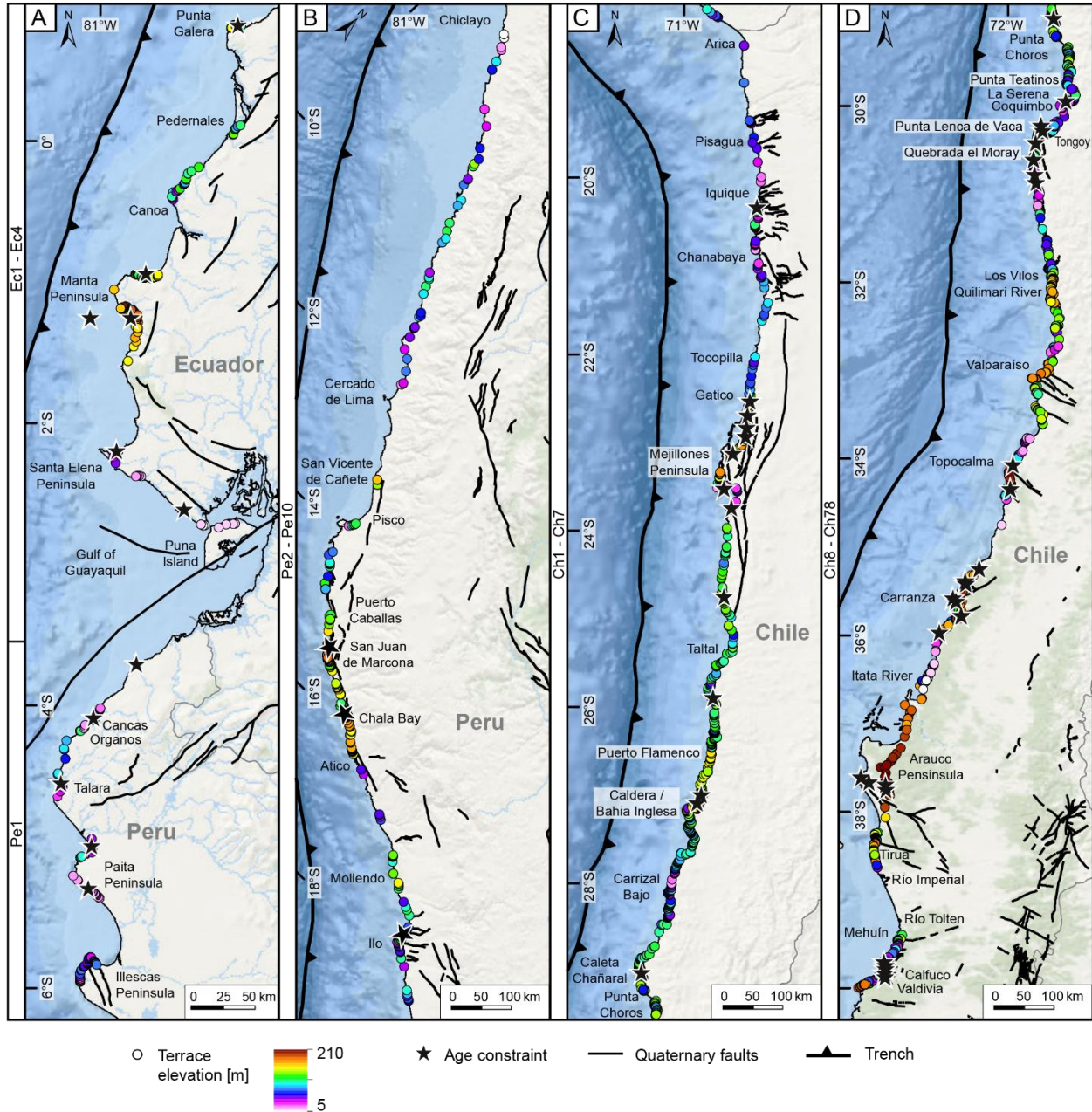
435 To evaluate the potential correlations between tectonic parameters and marine terraces, we analyzed the latitudinal
436 variability of these parameters projected along a curved “simple profile” and a 300-km-wide “swath profile” following
437 the trace of the trench. We used simple profiles for visualizing 2D data sets; for instance, to compare crustal faults
438 along the forearc area of the margin (Veloza et al., 2012; Melnick et al., 2020), we projected the seaward tip of each
439 fault. For the trench-sediment thickness, we projected discrete thickness estimates based on measurements from
440 seismic reflection profiles of Bangs and Cande (1997), Collot et al. (2002), Huene et al. (1996), and Schweller et al.
441 (1981). Finally, we projected the discrete trench distances from the point locations of our marine terrace measurements
442 along a simple profile. To compare bathymetric features on the oceanic plate, we used a compilation of bathymetric
443 measurements at 450 m resolution (GEBCO Bathymetric Compilation Group, 2020). The data set was projected along
444 a curved, 300-km-wide swath profile using TopoToolbox (Schwanghart and Kuhn, 2010).

445 Finally, to elucidate the influence of climatic factors on marine terrace morphology, we compared the elevation, but
446 also the number of measurements as a proxy for preservation and exposure of marine terraces. We calculated wave
447 heights, tidal ranges, and reference water levels at the point locations of our marine terrace measurements using the
448 Indicative Meaning Calculator (IMCalc) from Lorscheid and Rovere (2019). We used the maximum values of the
449 hourly significant wave height, and for the tidal range we calculated the difference between the highest and lowest
450 astronomical tide. The reference water level represents the averaged position of the paleo sea level with respect to the
451 shoreline-angle elevation and, together with the indicative range (uncertainty), quantifies the indicative meaning
452 (Lorscheid and Rovere, 2019). We furthermore used the high-resolution data set of Ceccherini et al. (2015) for mean
453 annual precipitation, and we compared the azimuth of the coast in order to evaluate its exposure to wind and waves.
454 To facilitate these comparisons, we extracted the values of all these parameters at the point locations of our marine
455 terrace measurements and projected them along a simple profile. Calculations and outputs were processed and
456 elaborated using MATLAB® 2020b.

457 **4. Results**

458 **4.1. Marine terrace geomorphology and shoreline-angle elevations**

459 In the following sections we describe our synthesized database of last interglacial marine terrace elevations along the
460 WSAC. Marine terraces of the last interglacial are generally well preserved and almost continuously exposed along
461 the WSAC, allowing ^{to} ~~us~~ estimate ^{of} ~~the~~ elevations with a high spatial density. To facilitate the descriptions of marine terrace-
462 elevation patterns, we divided the coastline into four sectors based on their main geomorphic characteristics (Fig. 5):
463 1) the Talara bend in northern Peru and Ecuador, 2) southern and central Peru, 3) northern Chile, and 4) central and
464 south-central Chile. In total we carried out 1,843 MIS-5e terrace measurements with a median elevation of 30.1 m asl
465 and 110 MIS-5c terrace measurements with a median of 38.6 m. The regions with exceptionally high marine terrace
466 elevations (≥ 100 m) comprise the Manta Peninsula in Ecuador, the San Juan de Marcona area in south-central Peru,
467 and three regions in south-central Chile (Topocalma, Carranza, and Arauco). Marine terraces at high altitudes (≥ 60
468 m) can also be found in Chile on the Mejillones Peninsula, south of Los Vilos, near Valparaíso, in Tirua, and near
469 Valdivia, while terrace levels only slightly above the median elevation are located at Punta Galera in Ecuador, south
470 of Puerto Flamenco, at Caldera/Bahía Inglesa, near Caleta Chañaral, and near the Quebrada El Moray in the Altos de
471 Talinay area in Chile. In the following sections we describe the characteristics of each site in detail, the names of the
472 sites are written in brackets following the same nomenclature as in the WALIS database (i.e., Pe – Peru, Ec – Ecuador,
473 Ch – Chile).



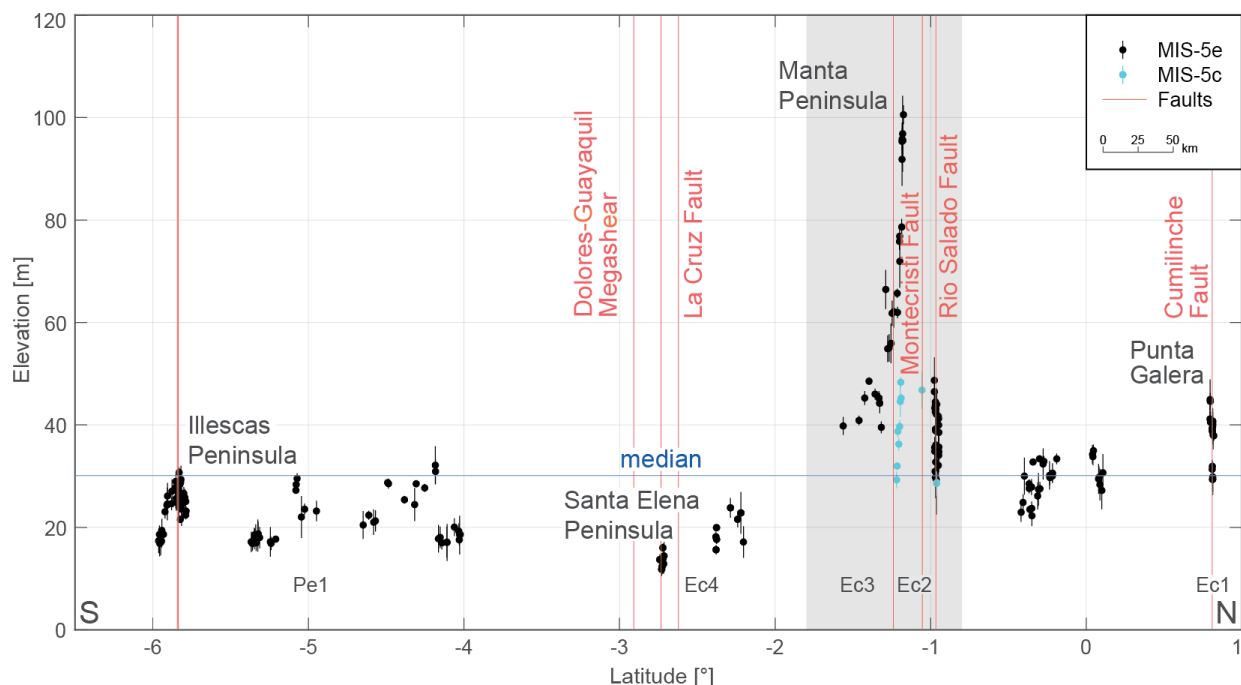
474

475 **Figure 5. Shoreline-angle elevation measurements (colored points), referencing points (black stars), Quaternary faults (bold**
 476 **black lines) (Veloza et al., 2012; Melnick et al., 2020), and locations mentioned in the text for the four main geomorphic**
 477 **segments (for location see Fig. 1A) (World Ocean Basemap: Esri, Garmin, GEBCO, NOAA NGDC, and other contributors).**
 478 **Site names referring to the entries in the WALIS database are on the left margin of each sub-figure (Pe – Peru, Ec –**
 479 **Ecuador, Ch – Chile). (A) Talara bend in Ecuador and northern Peru. (B) Central and southern Peru. (C) Northern Chile.**
 480 **(D) Central and south-central Chile.**

481 **4.1.1. Ecuador and northern Peru (1°N–6.5°S)**

482 The MIS-5e terrace levels in Ecuador and northern Peru [sites Ec1 to Ec4 and Pe1] are discontinuously preserved
 483 along the coast (Fig. 6). They often occur at low elevations (between 12 m and 30 m) and show abrupt local changes

484 in elevation, reaching a maximum at the Manta Peninsula. Punta Galera in northern Ecuador displays relatively broad
 485 and well-preserved marine terraces ranging between 40 and 45 m elevation and rapidly decrease eastward to about 30
 486 m asl across the Cumilínche fault [Ec1]. Farther south, between Pedernales and Canoa [Ec1], narrow terraces occur
 487 at lower altitudes of 22–34 m asl. A long-wavelength (~120 km) pattern in terrace-elevation change can be observed
 488 across the Manta Peninsula with the highest MIS-5e terraces peaking at ~100 m asl at its southern coast [Ec2]. This
 489 terrace level is hardly visible in its highest areas with platform widths smaller than 100 m due to deeply incised and
 490 narrowly spaced river valleys. We observe lower and variable elevations between 30 and 50 m across the Rio Salado
 491 fault in the San Mateo paleo-gulf in the north, while the terrace elevations increase gradually from ~40 m in the Pile
 492 paleo-gulf in the south [Ec3] toward the center of the peninsula (El Aromo dome) and the Montecristi fault [Ec3]. A
 493 lower terrace level correlated to MIS-5c displays similar elevation patterns as MIS-5e within the Pile paleo-gulf and
 494 areas to the north. Near the Gulf of Guayaquil and the Dolores-Guayaquil megashear, the lowest terrace elevations
 495 occur at the Santa Elena Peninsula ranging between 17 and 24 m asl and even lower altitudes in its southern part, and
 496 on the Puna Island ranging between 11 and 16 m asl [Ec4]. In northern Peru [Pe1], we observe dismembered MIS-5e
 497 terraces in the coastal area between Cancas and Talara below the prominent Mancora Tablazo. “Tablazo” is a local
 498 descriptive name used in northern Peru (~3.5–6.5°S) for marine terraces that cover a particularly wide surface area
 499 (Pedoja et al., 2006b). South of Cancas, MIS-5e terrace elevations range between 17 and 20 m asl, reaching 32 m near
 500 Organos, and vary between 20 and 29 m in the vicinity of Talara. In the southward continuation of the Talara harbor,
 501 the Talara Tablazo widens, with a lower marine terrace at about 23 m asl immediately north of Paita Peninsula reaching
 502 30 m asl in the northern part of the peninsula. The last occurrence of well-preserved MIS-5e terraces in this sector
 503 exists at the Illescas Peninsula, where terrace elevations decrease from around 30 m to 17 m asl southward.



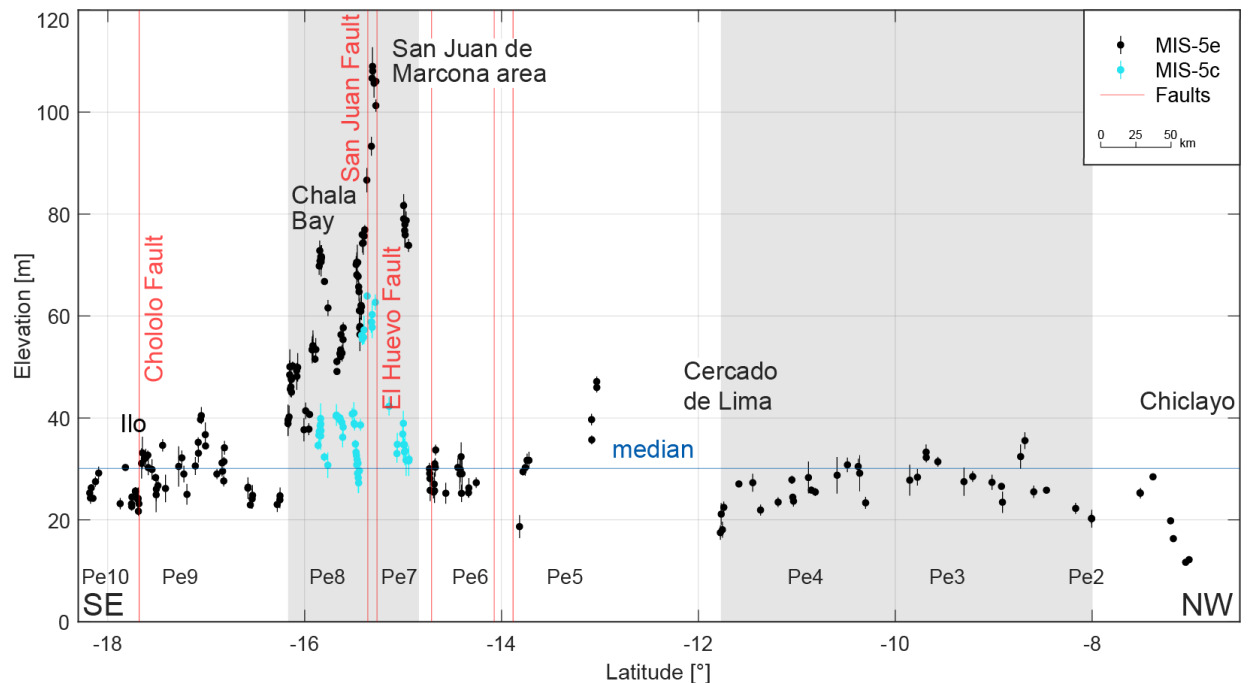
504
 505 **Figure 6. Measured shoreline-angle elevations of MIS-5e and 5c in Ecuador (Ec) and northern Peru (Pe). A high and**
 506 **inferred long-wavelength change in terrace elevation occurs at the Manta Peninsula (gray area) and at low elevations**

507 farther south at the Santa Elena Peninsula. Several terrace-elevation changes over short distances coincide with faulting at
508 Punta Galera and on the Illescas Peninsula. Median elevation: 30.1 m. For location see Fig. 5A.

509 4.1.2. Central and southern Peru (6.5°–18.3°S)

510 This segment comprises marine terraces at relatively low and constant elevations, but which are rather discontinuous
511 [sites Pe2 to Pe10], except in the San Juan de Marcona area, where the terraces increase in elevation drastically (Fig.
512 7). The coast in north-central Peru exhibits poor records of MIS-5e marine terraces, characterized by mostly narrow
513 and discontinuous remnants that are sparsely distributed along the margin with limited age constraints. Marine terraces
514 increase in elevation from 11 to 35 m asl south of Chiclayo [Pe2] and decrease to 17 m asl near Cercado de Lima [Pe3,
515 Pe4], forming a long-wavelength (~600 km), small amplitude (~20 m) upwarped structure. The MIS-5e terrace levels
516 are better expressed in the south-central and southern part of Peru at elevations between 35 and 47 m asl in San Vicente
517 de Cañete, decreasing to approximately 30 m asl in the vicinity of Pisco [Pe5]. South of Pisco, the coastal area becomes
518 narrow with terrace elevations ranging between 25 and 34 m asl [Pe6] and increasing abruptly to 74–79 m near Puerto
519 Caballas and the Río Grande delta. MIS-5e terrace elevations are highest within the San Juan de Marcona area,
520 reaching 109–93 m at Cerro Huevo and 87–56 m at Cerro Trés Hermanas [Pe7]. These higher terrace elevations
521 coincide with a wider coastal area, a better-preserved terrace sequence, and several crustal faults, such as the San Juan
522 and El Huevo faults.

523 Terrace heights west of Yauca indicate a further decrease to 50–58 m before a renewed increase to 70–72 m can be
524 observed in the Chala embayment [Pe8]. We observe a similar trend in elevation changes for the shoreline angles
525 attributed to the MIS-5c interglacial within the previously described high-elevation area: 31–39 m near the Río Grande
526 delta, 62–58 m below the Cerro Huevo peak, 64–27 m below the Cerro Trés Hermanas peak [Pe7], 36–40 m near
527 Yauca, and 34–40 m within the Chala embayment [Pe8]. Besides various changes in between, terrace elevations
528 decrease slowly from 54 m south of the Chala region to 38 m near Atico [Pe8]. The overall decrease south of the San
529 Juan de Marcona area therefore contrasts strikingly with the sharper decrease to the north. These high-elevation marine
530 terraces, which extend ~250 km along the coast from north of the San Juan de Marcona area to south of Chala Bay,
531 constitute one of the longest wavelength structures of the WSAC. Southeast of Atico, less well-preserved marine
532 terraces appear again in form of small remnants in a narrower coastal area. Starting with elevations as low as 24 m,
533 MIS-5e terrace altitudes increase southeastward to up to 40 m near Mollendo [Pe9], before they slightly decrease
534 again. The broader and quite well-preserved terraces of the adjacent Ilo area resulted in a smooth increase from values
535 greater than 25 m to 33 m and a sudden decrease to as low as 22 m across the Chololo fault [Pe9]. North of the Arica
536 bend, shoreline-angle measurements yielded estimates of 24–29 m in altitude [Pe10].

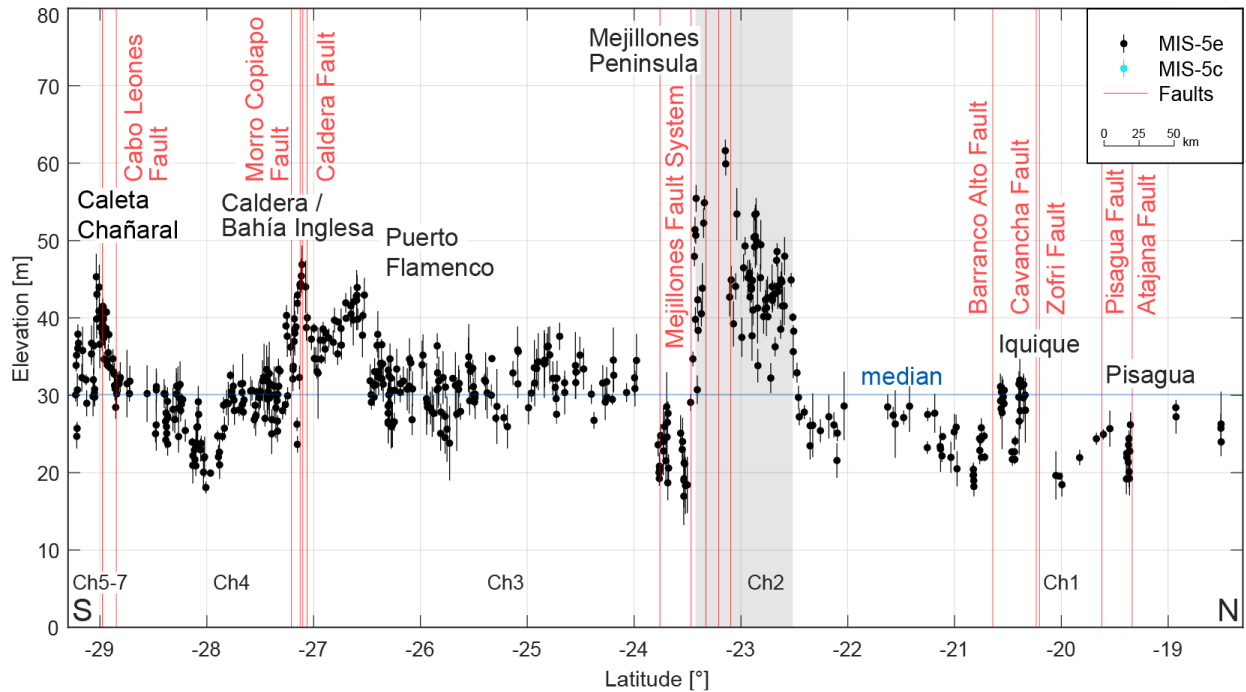


537
 538 **Figure 7. Measured shoreline-angle elevations of MIS-5e and 5c terraces in central and southern Peru (Pe). While only**
 539 **sparingly preserved terraces below the median (30.1 m) occur in central Peru between Chiclayo and Lima, a relatively broad**
 540 **and asymmetric distribution of marine terraces characterizes the area of San Juan de Marcona. For location see Fig. 5B.**

541 **4.1.3. Northern Chile (18.3°–29.3°S)**

542 Along the northern Chilean coast, marine terraces of the MIS-5e are characterized by a variable elevation pattern and
 543 the occurrence of numerous crustal faults associated with the Atacama fault system, although the changes in terrace
 544 elevation are not as pronounced as in the northern segments (Fig. 8) [sites Ch1 to Ch7]. The local widening of the
 545 coastal area near the Arica bend narrows southward with MIS-5e terraces at elevations of between 24 and 28 m asl in
 546 northernmost Chile [Ch1]. Just north of Pisagua, we measured shoreline-angle elevations of well-preserved marine
 547 terraces between 19 and 26 m across the Atajana fault [Ch1]. An areally limited zigzag pattern starting with shoreline-
 548 angle elevation values of 32 m south of Iquique and south of the Zofri and Cavanca faults decreases rapidly to
 549 approximately 22 m, but increases again to similar altitudes and drops as low as 18 m toward Chanabaya south of the
 550 Barranco Alto fault [Ch1]. A gentle, steady rise in terrace elevations can be observed south of Tocopilla where
 551 altitudes of 25 m are attained. South of Gatico, terrace markers of the MIS-5e highstand increase and continue
 552 northward for much of the Mejillones Peninsula within an approximate elevation range of 32–50 m asl, before reaching
 553 a maximum of 62 m asl at the Pampa de Mejillones [Ch2]. With its ~100 km latitudinal extent, we consider this
 554 terrace-elevation change to be a medium-wavelength structure. Although no MIS-5e terrace levels have been
 555 preserved at the Morro Mejillones Horst (Binnie et al., 2016), we measured shoreline-angle elevations at the elevated
 556 southwestern part of the peninsula that decrease sharply from 55 to 17 m asl in the vicinity of the Mejillones fault
 557 system [Ch2]. After a short interruption of the MIS-5e terrace level at Pampa Aeropuerto, elevations remain relatively
 558 low between 19–25 m farther south [Ch2]. Along the ~300-km coastal stretch south of Mejillones, marine terraces are
 559 scattered along the narrow coastal area ranging between 25 and 37 m asl [Ch3]. South of Puerto Flamenco, MIS-5e

560 terrace elevations range between 40 and 45 m asl until Caldera and Bahía Inglesa [Ch4]. The MIS-5e marine terrace
 561 elevations decrease abruptly south of the Caldera fault and the Morro Copiapó (Morro Copiapó fault) to between 25
 562 and 33 m asl, reaching 20 m asl north of Carrizal Bajo [Ch4]. In the southernmost part of the northern Chilean sector,
 563 the MIS-5e terraces rise from around 30 m asl to a maximum of 45 m asl near the Cabo Leones fault [Ch4], before
 564 decreasing in elevation abruptly near Caleta Chañaral and Punta Choros [Ch5, Ch6, Ch7].

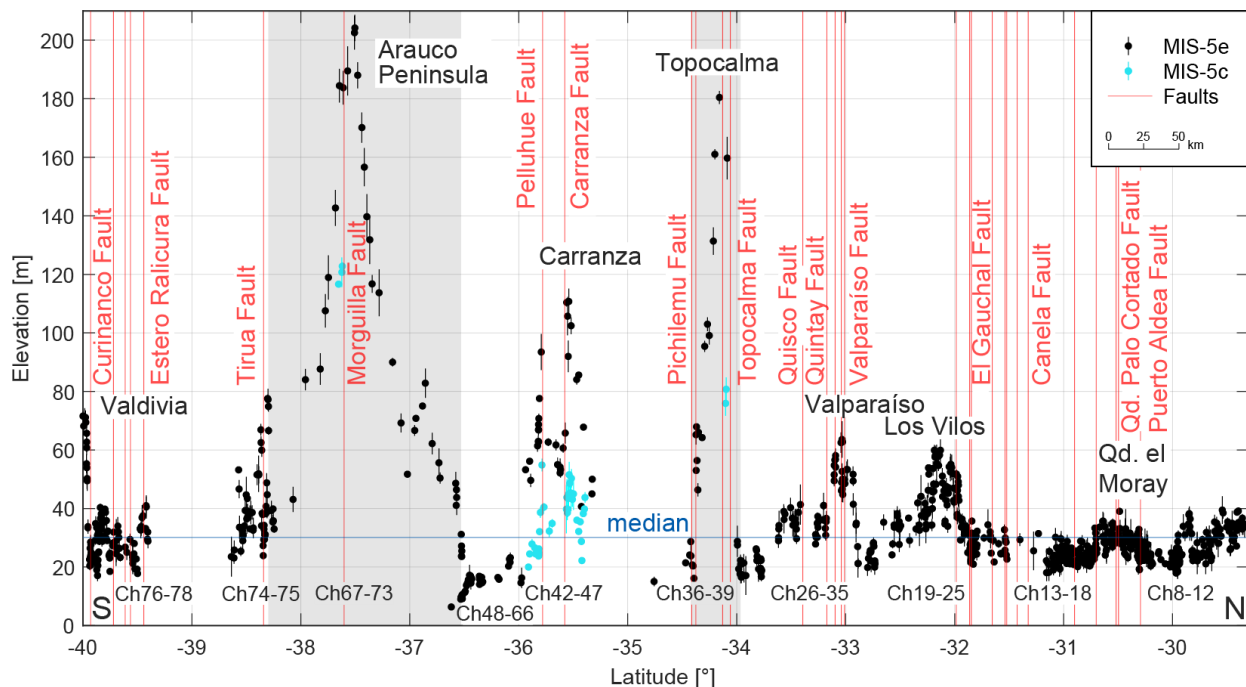


565 **Figure 8. Measured shoreline-angle elevations of MIS-5e and 5c terraces in northern Chile (Ch). Faults and asymmetrically**
 566 **uplifted marine terraces of up to 60 m elevation characterize the Mejillones Peninsula, reaching values below 20 m at the**
 567 **southern margin. Terrace elevations attain peak values south of Puerto Flamenco, at Caldera/Bahía Inglesa, and north of**
 568 **Caleta Chañaral, while in between minimum elevations below 20 m prevail (north of Carrizal Bajo). Median elevation is**
 569 **30.1 m. For location see Fig. 5C.**
 570

571 **4.1.4. Central Chile (29.3°–40°S)**

572 Marine terraces along central Chile display variable, high-amplitude terrace-elevation patterns associated with
 573 numerous crustal faults, and include a broad-scale change in terrace altitudes with the highest MIS-5e marine terrace
 574 elevations of the entire South American margin on the Arauco Peninsula (Fig. 9) [sites Ch8 to Ch78]. South of Punta
 575 Choros, marine terrace elevations decrease from values close to 40 to 22 m asl north of Punta Teatinos [Ch8, Ch9]. A
 576 maximum elevation of 40 m is reached by the terraces just south of this area [Ch10] whereas north of La Serena, a
 577 sharp decrease leads to values between 20 and 30 m for marine terraces south of Coquimbo Bay and in the Tongoy
 578 Bay area [Ch11, Ch12]. South of Punta Lengua de Vaca, our measurements of the exceptionally well-preserved
 579 staircase morphology of the terraces are within the same elevation range between 20 and 30 m, increasing slowly to
 580 40 m near the Quebrada el Moray [Ch13]. Although we could not observe a significant change in terrace elevation
 581 across the Puerto Aldea fault, we measured an offset of ~7 m across the Quebrada Palo Cortado fault. MIS-5e terrace
 582 levels decrease thereafter and vary between 20 and 30 m in altitude until north of Los Vilos [Ch14–Ch18], where they
 583 increase in elevation [Ch19], reaching 60 m near the Rio Quilimari [Ch20]. The marine terraces become wider in this

584 area and are associated with scattered sea stacks. Decreasing farther south to only 20 m asl [Ch21–Ch25], the coastal
 585 area narrows and has terrace heights of up to 64 m near Valparaíso, in an area that is cut by numerous faults (e.g.,
 586 Valparaíso and Quintay faults) [Ch26–Ch32]. Another low-elevation area follows southward, with values as low as
 587 17 m [Ch33–Ch35]. Farther south, between 34°S and 38°S, broad (~200 km at Arauco), medium (~45 km at
 588 Topocalma), and narrow (Carranza) upwarped zones occur that are manifested by variable terrace elevations. These
 589 include prominent high-terrace elevations at Topocalma with a maximum of 180 m [Ch36–Ch39], slightly lower levels
 590 of 110 m at Carranza [Ch42–Ch47], exceptionally low values near the Río Itata (< 10 m) [Ch48–Ch64, Ch66], and
 591 the most extensive and highest shoreline-angle elevations on the Arauco Peninsula with elevations in excess of 200 m
 592 [Ch67–Ch73]. Additionally, we measured MIS-5c terrace elevations in the three higher exposed areas with a range of
 593 20–55 m at Carranza, and a few locations at Topocalma (76–81 m) and Arauco (117–123 m). The medium-wavelength
 594 structure of Topocalma is bounded by the Pichilemu and Topocalma faults, and near Carranza several fault offsets
 595 (e.g., Pelluhue and Carranza faults) are responsible for the short-wavelength changes in terrace elevation. In contrast,
 596 crustal faulting is nearly absent in the high-elevation and long-wavelength structure at Arauco. MIS-5e terrace
 597 elevations are highly variable within a short area south of the Arauco Peninsula near the Tirua fault, increasing rapidly
 598 from 27 m to 78 m and decreasing thereafter to approximately 20 m [Ch74, Ch75]. The continuity of terraces is
 599 interrupted by the absence of terrace levels between Río Imperial and Río Toltén, but resumes afterward with a highly
 600 frequent zigzag pattern and multiple faults (e.g., Estero Ralicura and Curinanco faults) from as low as 18 m to a
 601 maximum of 40 m [Ch76, Ch77]. In this area locations with the highest terrace levels comprise the terraces near
 602 Mehuín and Calfuco. A final increase in shoreline-angle elevations from about 20–30 m up to 76 m near Valdivia
 603 coincides with the southern terminus of our terrace-elevation measurements [Ch78].



604
 605 **Figure 9. Measured shoreline-angle elevations of MIS-5e and 5c terraces in central Chile (Ch). Extensive faulting coincides**
 606 **with various high terrace elevations of the last interglacial highstand north of Los Vilos, near Valparaíso, at Topocalma,**
 607 **Carranza, and near Valdivia. The most pronounced and long-wavelength change in terrace elevation occurs on the Arauco**

608 **Peninsula with maximum elevations over 200 m and minimum elevations below 10 m north of Concepción. Qd. – Quebrada.**
609 **Median elevation: 30.1 m. For location see Fig. 5D.**

610 **4.2. Statistical analysis**

611 Our statistical analysis of mapped shoreline-angle elevations resulted in a maximum kernel density at 28.96 m with a
612 95% confidence interval from 18.59 m to 67.85 m (2σ) for the MIS-5e terrace level (Fig. 10A). The MIS-5c terrace
613 yielded in a maximum kernel density at a higher elevation of 37.20 m with 2σ ranging from 24.50 m to 63.92 m. It is
614 important to note that the number of MIS-5c measurements is neither as high nor as continuous as compared to that
615 of the MIS-5e level. MIS-5c data points were measured almost exclusively in sites where MIS-5e reach high elevations
616 (e.g., San Juan de Marcona with MIS-5e elevations between 40 and 110 m).

617 The distribution of measurement errors was studied using probability kernel-density plots for each topographic
618 resolution (1-5 m LIDAR, 12 m TanDEM-X, and 30 m TanDEM-X). The three data sets display similar distributions
619 and maximum likelihood probabilities (MLP); for instance, LiDAR data show a MLP of 0.93 m, the 12 m TanDEM-
620 X a MLP of 1.16 m, and 30 m TanDEM-X a MLP of 0.91 m (Fig. 10B). We observe the lowest errors from the 30 m
621 TanDEM-X, slightly higher errors from the 1-5 m LiDAR data, and the highest errors from the 12 m TanDEM-X.
622 This observation is counterintuitive as we would expect lower errors for topographic data sets with higher resolution
623 (1-5 m LiDAR). The reason for these errors is probably related to the higher number of measurements using the 12 m
624 TanDEM-X (1564) in comparison with the measurements using 30 m TanDEM-X (50), which result in a higher
625 dispersion and a more realistic representation of the measurement errors (Fig. 10B). In addition, the relation between
626 terrace elevations and error estimates shows that comparatively higher errors are associated with higher terrace
627 elevations, although the sparse point density of high terrace-elevation measurements prevents a clear correlation from
628 being recognized (Fig. 10C).

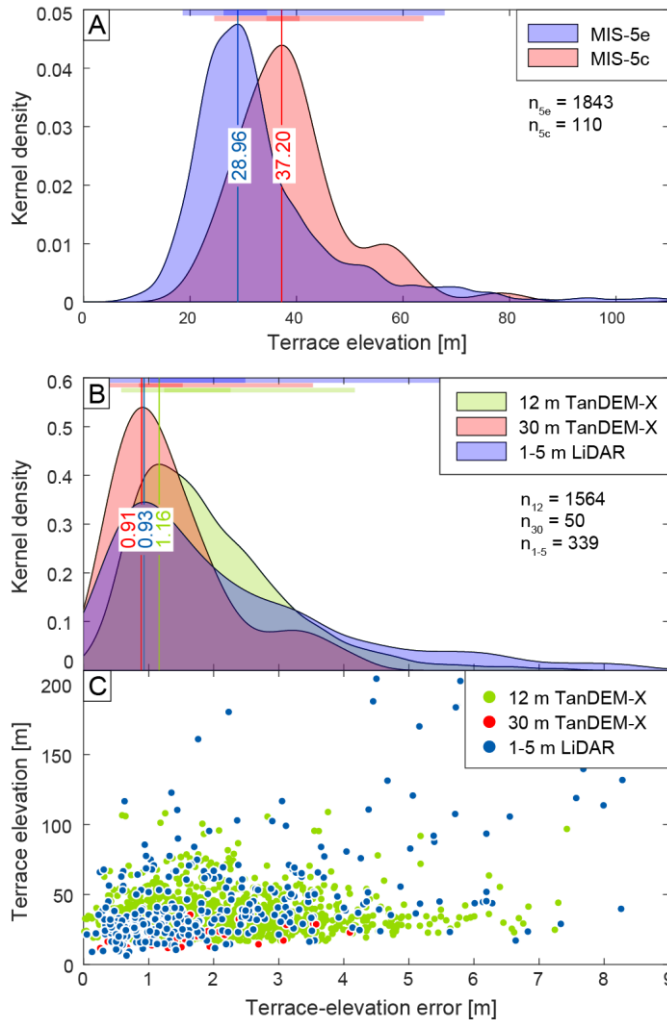


Figure 10. Statistical analysis of measured shoreline-angle elevations. (A) Kernel-density plot of MIS-5e and 5c terrace elevations with maximum likelihood probabilities (m.l.p.) at 28.96 m elevation for MIS-5e and 37.20 m elevation for MIS-5c (n : number of measurements). Colored bars on top highlight the standard deviations σ and 2σ . (B) Kernel-density and their associated standard-deviation (σ and 2σ) calculations of terrace-elevation errors for source DEMs of various resolutions. The most abundant 12 m TanDEM-X has a m.l.p.-error of 1.16 m, while the 30 m TanDEM-X and the 1-5 m LiDAR produce slightly lower errors of 0.91 m and 0.93 m, respectively. (C) Terrace-elevation errors plotted against terrace elevation for the individual source DEMs. Although the point density for high terrace elevations is low, a weak correlation of high errors with high terrace elevations can be observed.

629 4.3. Coastal uplift-rate estimates

630 We calculated uplift rates from 1953 terrace-elevation measurements of MIS-5e (1843) and MIS-5c (110) along the
 631 WSAC with a median uplift rate of approximately 0.22 m/ka (Fig. 11). As with the distribution of terrace elevations,
 632 we similarly observed several small-scale and large-scale, high-amplitude changes in uplift rate along the coast. The
 633 most pronounced long-wavelength highs ($\geq 1^\circ$ latitude) in uplift rate are located on the Manta Peninsula (0.79 m/ka),
 634 in the San Juan de Marcona area (0.85 m/ka), and on the Arauco Peninsula (1.62 m/ka). Medium-wavelength structures
 635 include the Mejillones Peninsula (0.47 m/ka) and Topocalma (1.43 m/ka), while shorter wavelength structures that
 636 are characterized by exceptionally high uplift rates seem to be limited to the central Chilean part of the coastline,
 637 especially between 31.5° and 40° S. The most striking example includes Carranza with an uplift rate of up to 0.87 m/ka
 638 since the formation of the oldest MIS-5 terrace levels. Lower, but still quite high, uplift rates were calculated for areas
 639 north of Los Vilos (0.46 m/ka), near Valparaíso (0.49 m/ka), and near Valdivia (0.59 m/ka). The lowest uplift rates
 640 along the South American margin occur at Penco immediately north of Concepción (0.03 m/ka), south of Chiclayo in
 641 northern Peru (0.07 m/ka), and on the southern Santa Elena Peninsula in Ecuador (0.07 m/ka).

But these values very spatially due to GIP (Summer et al, 2016)

642 **5. Discussion**

643 **5.1. Advantages and limitations of the database of last interglacial marine terrace elevations along the**
644 **WSAC**

645 In this study we generated a systematic database of last interglacial marine terrace elevations with unprecedented
646 resolution based on an almost continuous mapping of ~2,000 measurements along 5,000 km of the WSAC. This opens
647 up several possibilities for future applications in which this database can be used; for example, marine terraces are
648 excellent strain markers that can be used in studies on deformation processes at regional scale, and thus the synthesis
649 allows comparisons between deformation rates at different temporal scales in different sectors of the margin or
650 analyses linking specific climate-driven and tectonic coastal processes, and landscape evolution. However, there are
651 a number of limitations and potential uncertainties that can limit the use of this database in such studies without taking
652 several caveats into consideration.

653 One of the most critical limitations of using the database is associated with the referencing points used to tie our
654 marine terrace measurements, which are in turn based on the results and chronological constraints provided by
655 previous studies. The referencing points are heterogeneously distributed along the WSAC, resulting in some cases of
656 up to 600 km distance to the nearest constrained point, such as in Central Peru [e.g. Pe2]. This may have a strong
657 influence on the confidence in the measurement of the marine terrace elevation at these sites. In addition, the
658 geochronological control of some of the referencing points may be based on dating methods with pronounced
659 uncertainties (e.g., amino acid racemization, electron spin resonance, terrestrial cosmogenic radionuclides), which
660 may result in equivocal interpretations and chronologies of marine terrace levels. In order to address these potential
661 factors of uncertainty we defined a quality rating (see section 3.1.), which allows classifying our mapping results based
662 on their confidence and reliability. Therefore, by considering measurements above a defined quality it is possible to
663 increase the level of confidence for future studies using this database; however, this might result in a decrease of the
664 number of measurements available for analysis and comparison.

Also assumed no GIA in your upl. rate calc.

665 **5.2. Tectonic and climatic controls on the elevation and morphology of marine terraces along the WSAC**

666 In this section we provide a brief synthesis of our data set and its implications for coastal processes and overall
667 landscape evolution influenced by a combination of tectonic and climatic forcing factors. This synthesis emphasizes
668 the significance of our comprehensive data set for a variety of coastal research problems that were briefly introduced
669 in section 5.1. Our detailed measurements of marine terraces along the WSAC reveal variable elevations and a
670 heterogeneous distribution of uplift rates associated with patterns of short-, medium-, and long-wavelengths. In
671 addition, we observe different degrees of development of marine terraces along the margin expressed in variable
672 shoreline-angle density. There are several possible causes for this variability, which we explore by comparing terrace-
673 elevation patterns with different climatic and tectonic parameters.

674 **5.2.1. Tectonic controls on coastal uplift rates**

675 The spatial distribution of the MIS-5 marine terrace elevations along the convergent South American margin has
676 revealed several high-amplitude and long-wavelength changes with respect to tectonically controlled topography.
677 Long-wavelength patterns in terrace elevation ($\sim 10^2$ km) are observed at the Manta Peninsula in Ecuador, central Peru
678 between Chiclayo and Lima, San Juan de Marcona (Peru), and on the Arauco Peninsula in Chile, while medium-
679 wavelength structures occur at Mejillones Peninsula and Topocalma (Chile). Instead, short-wavelength patterns in
680 MIS-5 terrace elevations are observed, for instance, near Los Vilos, Valparaíso, and Carranza in Chile.

681 The subduction of bathymetric anomalies has been shown to exert a substantial influence on upper-plate deformation
682 (Fryer and Smoot, 1985; Taylor et al., 1987; Macharé and Ortlieb, 1992; Cloos and Shreve, 1996; Gardner et al., 2013;
683 Wang and Bilek, 2014; Ruh et al., 2016), resulting in temporally and spatially variable fault activity, kinematics, and
684 deformation rates (Mann et al., 1998; Saillard et al., 2011; Morgan and Bangs, 2017; Melnick et al., 2019). When
685 comparing the uplift pattern of MIS-5 marine terraces and the bathymetry of the oceanic plate, we observe that the
686 two long-wavelength structures in this area, on the Manta Peninsula and at San Juan de Marcona, both coincide with
687 the location of the subducting Nazca and Carnegie ridges, respectively (Fig. 11A and B); this was also previously
688 observed by other authors (Macharé and Ortlieb, 1992; Gutscher et al., 1999; Pedoja et al., 2006a; Saillard et al.,
689 2011). In summary, long-wavelength structures in coastal areas of the upper plate may be associated with deep-seated
690 processes (Melosh and Raefsky, 1980; Watts and Daly, 1981) possibly related to changes in the mechanical behavior
691 of the plate interface. In this context it is interesting that the high uplift rates on the Arauco Peninsula do not correlate
692 with bathymetric anomalies, which may suggest a different deformation mechanism. The scarcity of crustal faults
693 described in the Arauco area rather suggests that shallow structures associated with crustal bending and splay-faults
694 occasionally breaching through the upper crust (Melnick et al., 2012; Jara-Muñoz et al., 2015; Jara-Muñoz et al., 2017;
695 Melnick et al., 2019) may cause long-wavelength warping and uplift there (Fig. 11A).

696 In contrast, small-scale bathymetric anomalies correlate in part with the presence of crustal faults perpendicular to the
697 coastal margin near, for instance, the Juan Fernandez, Taltal, and Copiapó ridges (Fig. 11B); this results in short-
698 wavelength structures and a more localized altitudinal differentiation of uplifted terraces. This emphasizes also the
699 importance of last interglacial marine terraces as strain markers with respect to currently active faults, which might be
700 compared in the future with short-term deformation estimates from GPS or the earthquake catalog. In summary, short-
701 wavelength structures in the coastal realms of western South America may be associated with faults that root at shallow
702 depths within the continental crust (Jara-Muñoz et al., 2015; Jara-Muñoz et al., 2017; Melnick et al., 2019).

703 The thickness of sediment in the trench is an additional controlling factor on forearc architecture that may determine
704 which areas of the continental margin are subjected to subduction erosion or accretion (Hilde, 1983; Cloos and Shreve,
705 1988; Menant et al., 2020). Our data shows that the accretionary part of the WSAC (south of the intersection with the
706 Juan Fernandez Ridge at 32.9°S) displays faster median uplift rates of 0.26 m/ka than in the rest of the WSAC (Fig.
707 11B and C). However, no clear correlation is observed between trench fill, uplift rates, and the different structural
708 patterns in the erosive part of the margin. On the other hand, we observe lower uplift rates for greater distances from
709 the trench at the Arica bend, in central Peru, and in the Gulf of Guayaquil, while higher uplift rates occur in areas
710 closer to the trench, such as near the Nazca and Carnegie ridges and the Mejillones Peninsula.

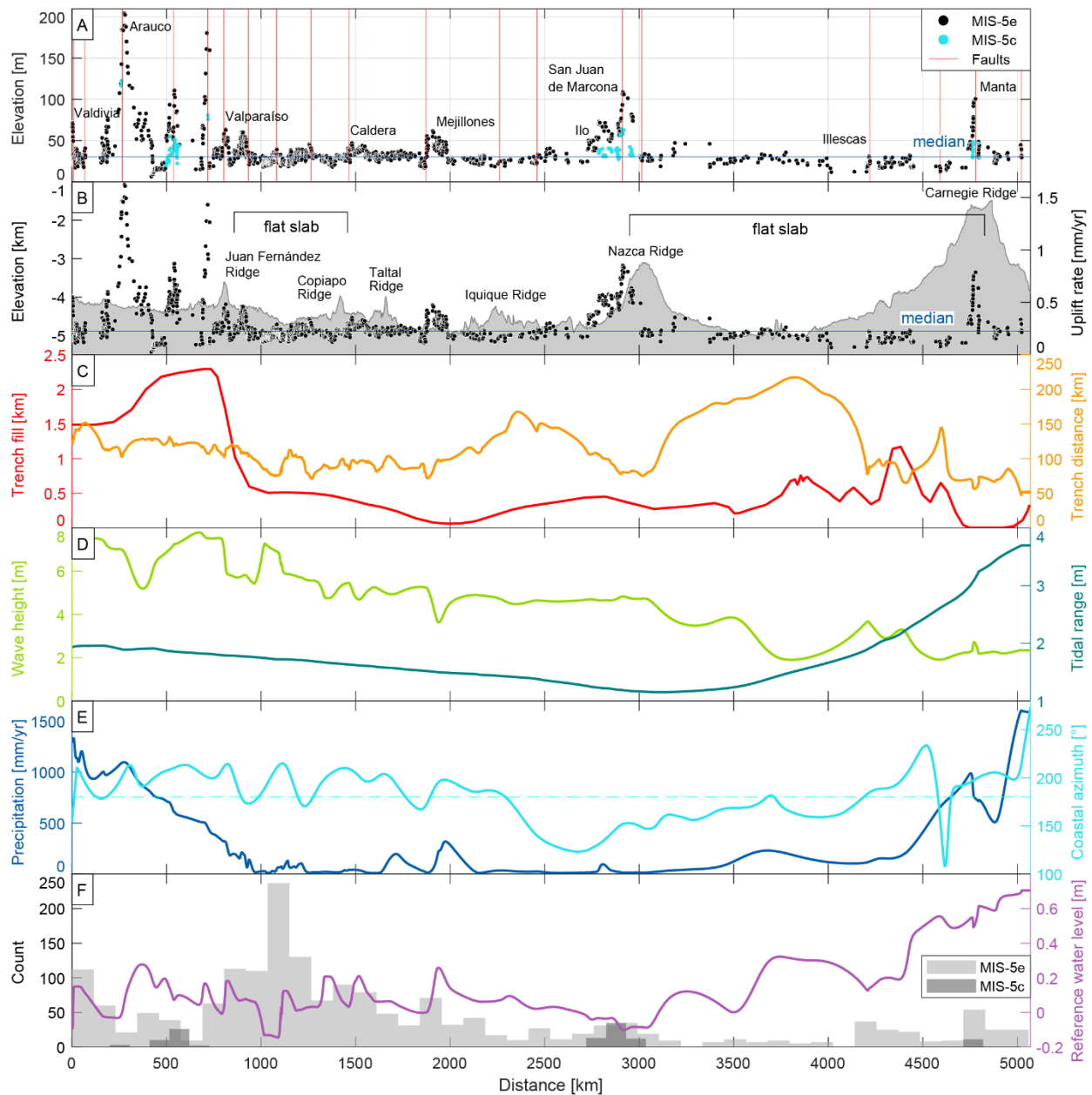
711 **5.2.2. Climatic controls on the formation and preservation of last interglacial marine terraces**

712 The latitudinal climate differences that characterize the western margin of South America may also control coastal
713 morphology and the generation and preservation of marine terraces (Martinod et al., 2016b). In order to evaluate the
714 influence of climate in the generation and/or degradation of marine terraces, we compared the number of marine
715 terrace measurements, which is a proxy for the degree of marine terrace preservation, and climatically controlled
716 parameters such as wave height, tidal range, coastline orientation, and the amount of precipitation.

717 The maximum wave height along the WSAC decreases northward from ~8 to ~2 m (see section 3.3, Fig. 11D).
718 Similarly, the tidal range decreases progressively northward from 2 to 1 m between Valdivia and San Juan de Marcona,
719 followed by a rapid increase to 4 m between San Juan de Marcona and the Manta Peninsula. We observe an apparent
720 correlation between the number of measurements and the tidal range in the north, between Illescas and Manta (Fig.
721 11F). Likewise, the increasing trend in the number of measurements southward matches with the increase in wave
722 height (Fig. 11D). An increase of wave height and tidal range may lead to enhanced erosion and morphologically well-
723 expressed marine terraces (Anderson et al., 1999; Trenhaile, 2002), which is consequently reflected in a higher number
724 of measurements that can be carried out. Furthermore, we observe low values for the reference water level (< 0.7 m)
725 resulting from tide and wave-height estimations in IMCalc (Lorscheid and Rovere, 2019), which are used to correct
726 our shoreline-angle measurements in the WALIS database (see section 3.3.).

727 The control of wave-erosion processes on the morphological expression of marine terraces may be counteracted by
728 erosional processes such as river incision. We note that the high number of preserved marine terraces between
729 Mejillones and Valparaíso decreases southward, which coincides with a sharp increase in mean annual precipitation
730 from 10 to 1000 mm/yr (Fig. 11E and F) and fluvial dissection. However, in the area with a high number of
731 measurements between the Illescas Peninsula and Manta we observe an opposite correlation: higher rainfall associated
732 with an increase of marine terrace preservation (Fig. 11E). This suggests that the interplay between marine terrace
733 generation and degradation processes apparently buffer each other, resulting in different responses under different
734 climatic conditions and coastal settings.

735 The higher number of marine terraces between Mejillones and Valparaíso and north of Illescas corresponds with a
736 SSW-NNE orientation of the coastline (azimuth between 200 and 220°). In contrast, NW-SE to N-S oriented coastlines
737 (azimuth between 125 and 180°), such as between the Arica and Huancabamba bends, correlate with a lower number
738 of marine terrace measurements (Fig. 11E and F). This observation appears, however, implausible considering that
739 NW-SE oriented coastlines may be exposed more directly to the erosive effect of storm waves associated with winds
740 approaching from the south. We interpret the orientation of the coastline therefore to be of secondary importance at
741 regional scale for the formation of marine terraces compared to other parameters, such as wave height, tidal range, or
742 rainfall.



743
 744 **Figure 11. Terrace-elevation and uplift-rate estimates plotted in comparison with various parameters (i.e., bathymetry,**
 745 **trench fill, trench distance, wave height, tidal range, precipitation, and coastal azimuth) that might influence the disparate**
 746 **characteristics of the marine terrace distribution revealed by our data set. We projected these parameters, elevations, and**
 747 **uplift rates with respect to a S-N-oriented polyline that represents the trench. (A) Terrace-elevation measurements and**
 748 **most important crustal faults (Veloza et al., 2012; Melnick et al., 2020). This shows the range of altitudes in different regions**
 749 **along the coast and possible relationships between terrace elevation and crustal faulting. The blue horizontal line indicates the**
 750 **median elevation (30.1 m). (B) Coastal uplift rates and mean bathymetry (GEBCO Bathymetric Compilation Group,**
 751 **2020) of a 150-km-swath west of the trench. The blue horizontal line indicates the median uplift rate (0.22 mm/a). (C)**
 752 **Sediment thickness of trench-fill deposits (red) (Bangs and Cande, 1997) and the distance of the trench from our terrace**
 753 **measurements (orange). Flat-slab segments of the subducting Nazca plate are indicated for central Chile and Peru. (D)**
 754 **Maximum wave heights along the WSAC (light green) and the tidal range (dark green) between highest and lowest**
 755 **astronomical tides (Lorscheid and Rovere, 2019). (E) Precipitation (blue) along the WSAC (Ceccherini et al., 2015) and**
 756 **azimuthal orientation of the coastline (cyan). (F) Histogram of terrace-elevation measurements along the WSAC.**

757 **6. Conclusions**

758 We measured 1,953 shoreline-angle elevations as proxies for paleo-sea levels of the MIS-5e and 5c terraces along
759 ~5,000 km of the WSAC between Ecuador and Southern Chile. Our measurements are based on a systematic
760 methodology and the resulting data have been standardized within the framework of the WALIS database. Our
761 mapping was tied using referencing points based on previously published terrace-elevation estimates and age
762 constraints that are summarized in the compilation of Pedoja et al. (2011). The limitations of this database are
763 associated with the temporal accuracy and spatial distribution of the referencing points, which we attempt to consider
764 by providing a quality-rating value to each measurement. The marine terrace elevations display a median value of
765 30.1 m for the MIS-5e level and a median uplift rate of 0.22 m/ka for MIS-5e and 5c. The lowest terrace elevations
766 and uplift rates along the entire WSAC occur immediately north of Concepción in Chile (6 m, 0.03 m/ka), south of
767 Chiclayo in northern Peru, and on the Santa Elena Peninsula in Ecuador (both 12 m, 0.07 m/ka). The regions with
768 exceptionally high marine terrace elevations (≥ 100 m) comprise the Manta Peninsula in Ecuador, the San Juan de
769 Marcona area in south-central Peru, and three regions in south-central Chile (Topocalma, Carranza, and Arauco).

770 The pattern of terrace elevations displays short-, medium- and long-wavelength structures controlled by a combination
771 of various mechanisms. Long-wavelength structures may be controlled by deep-seated processes at the plate interface,
772 such as the subduction of major bathymetric anomalies (e.g. Manta Peninsula and San Juan de Marcona region). In
773 contrast, short- and medium-wavelength deformation patterns may be controlled by crustal faults rooted within the
774 upper plate (e.g., between Mejillones and Valparaíso).

775 Latitudinal climate characteristics along the WSAC may influence the generation and preservation of marine terraces.
776 An increase in wave height and tidal range generally results in enhanced erosion and morphologically well-expressed,
777 sharply defined marine terraces, which correlates with the southward increase in the number of our marine terrace
778 measurements. Conversely, river incision and lateral scouring in areas with high precipitation may degrade marine
779 terraces, thus decreasing the number of potential marine terrace measurements, such as observed south of Valparaíso.

780
781 *Data availability.* The South American database of last interglacial shoreline-angle elevations is available online at
782 <http://doi.org/10.5281/zenodo.4309748> (Freisleben et al., 2020). The description of the WALIS-database fields can
783 be found at <https://doi.org/10.5281/zenodo.3961543> (Rovere et al., 2020).

784
785 *Author contributions.* The main compilers of the database were R.F., J.M.M., and J.J. The paper was written by R.F.
786 with significant input from J.J., D.M., M.S. regarding interpretation and further improvements of graphical data
787 representation.

788
789 *Acknowledgments.* We thank Alessio Rovere for his assistance with the WALIS database. The WALIS database was
790 developed by the ERC Starting Grant “Warmcoasts” (ERC-StG-802414) and PALSEA. PALSEA is a working group
791 of the International Union for Quaternary Sciences (INQUA) and Past Global Changes (PAGES), which in turn
792 received support from the Swiss Academy of Sciences and the Chinese Academy of Sciences. The structure of the
793 database was designed by A. Rovere, D. Ryan, T. Lorscheid, A. Dutton, P. Chutcharavan, D. Brill, N. Jankowski, D.
794 Mueller, M. Bartz, E.J. Gowan and K. Cohen. This study was supported by the Millennium Scientific Initiative of the
795 Chilean government through grant NC160025 “Millennium Nucleus CYCLO The Seismic Cycle Along Subduction
796 Zones”, Chilean National Fund for Development of Science and Technology (FONDECYT) grants 1181479 and
797 1190258, the ANID PIA Anillo ACT192169. R.F. was supported by a research grant of Deutsche

798 Forschungsgemeinschaft to M.S. (DFG STR373/41-1). Constructive reviews by V. Regard and P.M. Figueiredo
799 helped to improve the paper.

800

801 **7. References**

802 Anderson, R.S., Densmore, A.L., Ellis, M.A., 1999. The generation and degradation of marine terraces. *Basin*
803 *Research* 11(1), 7–19. doi:10.1046/j.1365-2117.1999.00085.x.

804 Angermann, D., Klotz, J., Reigber, C., 1999. Space-geodetic estimation of the Nazca-South America Euler vector.
805 *Earth and Planetary Science Letters* 171(3), 329–334. doi:10.1016/S0012-821X(99)00173-9.

806 Baker, A., Allmendinger, R.W., Owen, L.A., Rech, J.A., 2013. Permanent deformation caused by subduction
807 earthquakes in northern Chile. *Nature Geoscience* 6(6), 492–496. doi:10.1038/ngeo1789.

808 Bangs, N.L., Cande, S.C., 1997. Episodic development of a convergent margin inferred from structures and
809 processes along the southern Chile margin. *Tectonics* 16(3), 489–503.

810 Barazangi, M., Isacks, B.L., 1976. Spatial distribution of earthquakes and subduction of the Nazca plate beneath
811 South America. *Geology* 4(11), 686. doi:10.1130/0091-7613(1976)4<686:SDOEAS>2.0.CO;2.

812 Beck, S., Barrientos, S., Kausel, E., Reyes, M., 1998. Source characteristics of historic earthquakes along the central
813 Chile subduction zone. *Journal of South American Earth Sciences* 11(2), 115–129. doi:10.1016/S0895-
814 9811(98)00005-4.

815 Bendix, J., Rollenbeck, R., Reudenbach, C., 2006. Diurnal patterns of rainfall in a tropical Andean valley of
816 southern Ecuador as seen by a vertically pointing K-band Doppler radar. *International Journal of Climatology*
817 26(6), 829–846. doi:10.1002/joc.1267.

818 Bernhardt, A., Hebbeln, D., Regenberg, M., Lückge, A., Strecker, M.R., 2016. Shelfal sediment transport by an
819 undercurrent forces turbidity-current activity during high sea level along the Chile continental margin. *Geology*
820 44(4), 295–298. doi:10.1130/G37594.1.

821 Bernhardt, A., Schwanghart, W., Hebbeln, D., Stuut, J.-B.W., Strecker, M.R., 2017. Immediate propagation of
822 deglacial environmental change to deep-marine turbidite systems along the Chile convergent margin. *Earth and*
823 *Planetary Science Letters* 473, 190–204. doi:10.1016/j.epsl.2017.05.017.

824 Bilek, S.L., 2010. Invited review paper: Seismicity along the South American subduction zone: Review of large
825 earthquakes, tsunamis, and subduction zone complexity. *Tectonophysics* 495(1-2), 2–14.
826 doi:10.1016/j.tecto.2009.02.037.

827 Bilek, S.L., Schwartz, S.Y., DeShon, H.R., 2003. Control of seafloor roughness on earthquake rupture behavior.
828 *Tectonics* 31(5), 455. doi:10.1130/0091-7613(2003)031<0455:COSROE>2.0.CO;2.

829 Binnie, A., Dunai, T.J., Binnie, S.A., Victor, P., González, G., Bolten, A., 2016. Accelerated late quaternary uplift
830 revealed by ¹⁰Be exposure dating of marine terraces, Mejillones Peninsula, northern Chile. *Quaternary*
831 *Geochronology* 36, 12–27. doi:10.1016/j.quageo.2016.06.005.

832 Bookhagen, B., Strecker, M.R., 2008. Orographic barriers, high-resolution TRMM rainfall, and relief variations
833 along the eastern Andes. *Geophysical Research Letters* 35(6), 139. doi:10.1029/2007GL032011.

834 Cahill, T., Isacks, B.L., 1992. Seismicity and shape of the subducted Nazca Plate. *Journal of Geophysical Research*
835 97(B12), 17503. doi:10.1029/92JB00493.

836 Ceccherini, G., Ameztoy, I., Hernández, C., Moreno, C., 2015. High-Resolution Precipitation Datasets in South
837 America and West Africa based on Satellite-Derived Rainfall, Enhanced Vegetation Index and Digital Elevation
838 Model. *Remote Sensing* 7(5), 6454–6488. doi:10.3390/rs70506454.

839 Cembrano, J., Lavenue, A., Yañez, G., Riquelme, R., García, M., González, G., Hérial, G., 2007. Neotectonics. In:
840 Moreno, T., Gibbons, W. (Eds.), *The geology of Chile*. Geological Society, London, pp. 231–261.

841 Clift, P., Vannucchi, P., 2004. Controls on tectonic accretion versus erosion in subduction zones: Implications for
842 the origin and recycling of the continental crust. *Reviews of Geophysics* 42(2), 19. doi:10.1029/2003RG000127.

843 Clift, P.D., Hartley, A.J., 2007. Slow rates of subduction erosion and coastal underplating along the Andean margin
844 of Chile and Peru. *Geology* 35(6), 503. doi:10.1130/G23584A.1.

845 Cloos, M., Shreve, R.L., 1988. Subduction-channel model of prism accretion, melange formation, sediment
846 subduction, and subduction erosion at convergent plate margins: 1. Background and description. *Pure and*
847 *Applied Geophysics* 128(3-4), 455–500. doi:10.1007/BF00874548.

848 Cloos, M., Shreve, R.L., 1996. Shear-zone thickness and the seismicity of Chilean- and Marianas-type subduction
849 zones. *Geology* 24(2), 107. doi:10.1130/0091-7613(1996)024<0107:SZTATS>2.3.CO;2.

850 Collot, J.-Y., Charvis, P., Gutscher, M.-A., Operto, S., 2002. Exploring the Ecuador-Colombia Active Margin and
851 Interplate Seismogenic Zone. *Eos, Transactions, American Geophysical Union* 83(17), 185.
852 doi:10.1029/2002EO000120.

853 Collot, J.-Y., Sanclemente, E., Nocquet, J.-M., Leprêtre, A., Ribodetti, A., Jarrin, P., Chlieh, M., Graindorge, D.,
854 Charvis, P., 2017. Subducted oceanic relief locks the shallow megathrust in central Ecuador. *Journal of*
855 *Geophysical Research: Solid Earth* 122(5), 3286–3305. doi:10.1002/2016JB013849.

856 Costa, C., Alvarado, A., Audemard, F., Audin, L., Benavente, C., Bezerra, F.H., Cembrano, J., González, G., López,
857 M., Minaya, E., Santibañez, I., Garcia, J., Arcila, M., Pagani, M., Pérez, I., Delgado, F., Paolini, M., Garro, H.,
858 2020. Hazardous faults of South America; compilation and overview. *Journal of South American Earth Sciences*
859 104(1), 102837. doi:10.1016/j.jsames.2020.102837.

860 Costa, C., Machette, M.N., Dart, R.L., Bastias, H.E., Paredes, J.D., Perucca, L.P., Tello, G.E., Haller, K.M., 2000.
861 Map and database of Quaternary faults and folds in Argentina. Open-File Report. US Geological Survey.
862 <http://dx.doi.org/10.3133/ofr00108>.

863 Coudurier-Curveur, A., Lacassin, R., Armijo, R., 2015. Andean growth and monsoon winds drive landscape
864 evolution at SW margin of South America. *Earth and Planetary Science Letters* 414, 87–99.
865 doi:10.1016/j.epsl.2014.12.047.

866 DeMets, C., Gordon, R.G., Argus, D.F., 2010. Geologically current plate motions. *Geophysical Journal International*
867 181(1), 1–80. doi:10.1111/j.1365-246X.2009.04491.x.

868 Espurt, N., Funiciello, F., Martinod, J., Guillaume, B., Regard, V., Faccenna, C., Brusset, S., 2008. Flat subduction
869 dynamics and deformation of the South American plate: Insights from analog modeling. *Tectonics* 27(3), n/a-
870 n/a. doi:10.1029/2007TC002175.

871 Freisleben, R., Jara-Muñoz, J., Melnick, D., Martínez, J.M., Strecker, M., 2020. Marine terraces of the last
872 interglacial period along the Pacific coast of South America (1°N-40°S). Zenodo.
873 doi:10.5281/ZENODO.4309748.

874 Fryer, P., Smoot, N.C., 1985. Processes of seamount subduction in the Mariana and Izu-Bonin trenches. *Marine*
875 *Geology* 64(1-2), 77–90. doi:10.1016/0025-3227(85)90161-6.

876 Fuenzalida, H., Cooke, R., Paskoff, R., Segerstrom, K., Weischet, W., 1965. High Stands of Quaternary Sea Level
877 Along the Chilean Coast. *Geological Society of America Special Papers* 84, 473–496.

878 Gallen, S.F., Wegmann, K.W., Bohnenstiehl, D.R., Pazzaglia, F.J., Brandon, M.T., Fassoulas, C., 2014. Active
879 simultaneous uplift and margin-normal extension in a forearc high, Crete, Greece. *Earth and Planetary Science*
880 *Letters* 398, 11–24. doi:10.1016/j.epsl.2014.04.038.

881 Gardner, T.W., Fisher, D.M., Morell, K.D., Cupper, M.L., 2013. Upper-plate deformation in response to flat slab
882 subduction inboard of the aseismic Cocos Ridge, Osa Peninsula, Costa Rica. *Lithosphere* 5(3), 247–264.
883 doi:10.1130/L251.1.

884 Garreaud, R.D., 2009. The Andes climate and weather. *Advances in Geosciences* 22, 3–11. doi:10.5194/adgeo-22-3-
885 2009.

886 GEBCO Bathymetric Compilation Group, 2020. The GEBCO_2020 Grid - a continuous terrain model of the global
887 oceans and land. British Oceanographic Data Centre, National Oceanography Centre, NERC, UK.

888 Geersen, J., Ranero, C.R., Barckhausen, U., Reichert, C., 2015. Subducting seamounts control interplate coupling
889 and seismic rupture in the 2014 Iquique earthquake area. *Nature communications* 6, 8267.
890 doi:10.1038/ncomms9267.

891 German Aerospace Center (DLR), 2018. TanDEM-X - Digital Elevation Model (DEM) - Global, 12m.

- 892 González, G., Carrizo, D., 2003. Segmentación, cinemática y cronología relativa de la deformación tardía de la Falla
893 Salar del Carmen, Sistema de Fallas de Atacama, (23°40'S), norte de Chile. *Revista Geológica de Chile* 30(2).
894 doi:10.4067/S0716-02082003000200005.
- 895 Goy, J.L., Macharé, J., Ortlieb, L., Zazo, C., 1992. Quaternary shorelines in Southern Peru a record of global sea-
896 level fluctuations and tectonic uplift in Chala Bay. *Quaternary International* 15-16, 99–112.
- 897 Gutscher, M.-A., Malavieille, J., Lallemand, S., Collot, J.-Y., 1999. Tectonic segmentation of the North Andean
898 margin: impact of the Carnegie Ridge collision. *Earth and Planetary Science Letters* 168(3-4), 255–270.
899 doi:10.1016/S0012-821X(99)00060-6.
- 900 Gutscher, M.-A., Spakman, W., Bijwaard, H., Engdahl, E.R., 2000. Geodynamics of flat subduction: Seismicity and
901 tomographic constraints from the Andean margin. *Tectonics* 19(5), 814–833. doi:10.1029/1999TC001152.
- 902 Hampel, A., 2002. The migration history of the Nazca Ridge along the Peruvian active margin: a re-evaluation.
903 *Earth and Planetary Science Letters* 203(2), 665–679. doi:10.1016/S0012-821X(02)00859-2.
- 904 Hayes, G.P., Moore, G.L., Portner, D.E., Hearne, M., Flamme, H., Furtney, M., Smoczyk, G.M., 2018. Slab2, a
905 comprehensive subduction zone geometry model. *Science (New York, N.Y.)* 362(6410), 58–61.
906 doi:10.1126/science.aat4723.
- 907 Hearty, P.J., Hollin, J.T., Neumann, A.C., O’Leary, M.J., McCulloch, M., 2007. Global sea-level fluctuations during
908 the Last Interglaciation (MIS 5e). *Quaternary Science Reviews* 26(17-18), 2090–2112.
909 doi:10.1016/j.quascirev.2007.06.019.
- 910 Hilde, T.W.C., 1983. Sediment subduction versus accretion around the Pacific. *Tectonophysics* 99(2-4), 381–397.
911 doi:10.1016/0040-1951(83)90114-2.
- 912 Houston, J., Hartley, A.J., 2003. The central Andean west-slope rainshadow and its potential contribution to the
913 origin of hyper-aridity in the Atacama Desert. *International Journal of Climatology* 23(12), 1453–1464.
914 doi:10.1002/joc.938.
- 915 Hsu, J.T., 1992. Quaternary uplift of the Peruvian coast related to the subduction of the Nazca Ridge: 13.5 to 15.6
916 degrees south latitude. *Quaternary International* 15-16, 87–97. doi:10.1016/1040-6182(92)90038-4.
- 917 Hsu, J.T., Leonard, E.M., Wehmiller, J.F., 1989. Aminostratigraphy of Peruvian and Chilean Quaternary marine
918 terraces. *Quaternary Science Reviews* 8(3), 255–262. doi:10.1016/0277-3791(89)90040-1.
- 919 Huene, R. von, Pecher, I.A., Gutscher, M.-A., 1996. Development of the accretionary prism along Peru and material
920 flux after subduction of Nazca Ridge. *Tectonics* 15(1), 19–33. doi:10.1029/95TC02618.
- 921 Jaillard, E., Hérail, G., Monfret, T., Díaz-Martínez, E., Baby, P., Lavenue, A., Dumont, J.F., 2000. Tectonic evolution
922 of the Andes of Ecuador, Peru, Bolivia, and northernmost Chile. In: Cordani, U.G., Milani, E.J., Thomaz, F.A.,

- 923 Campos, D.A. (Eds.), Tectonic evolution of South America. Sociedad Brasileira de Geologia, Rio de Janeiro,
924 pp. 481–559.
- 925 Jara-Muñoz, J., Melnick, D., Brill, D., Strecker, M.R., 2015. Segmentation of the 2010 Maule Chile earthquake
926 rupture from a joint analysis of uplifted marine terraces and seismic-cycle deformation patterns. *Quaternary*
927 *Science Reviews* 113, 171–192. doi:10.1016/j.quascirev.2015.01.005.
- 928 Jara-Muñoz, J., Melnick, D., Socquet, A., Cortés-Aranda, J., Strecker, M.R., 2018. Slip rate and earthquake
929 recurrence of the Pichilemu Fault. *Congreso Geológico Chileno*, 15th.
- 930 Jara-Muñoz, J., Melnick, D., Strecker, M.R., 2016. TerraceM: A MATLAB® tool to analyze marine and lacustrine
931 terraces using high-resolution topography. *Geosphere* 12(1), 176–195. doi:10.1130/GES01208.1.
- 932 Jara-Muñoz, J., Melnick, D., Zambrano, P., Rietbrock, A., González, J., Argandoña, B., Strecker, M.R., 2017.
933 Quantifying offshore fore-arc deformation and splay-fault slip using drowned Pleistocene shorelines, Arauco
934 Bay, Chile. *Journal of Geophysical Research: Solid Earth* 122(6), 4529–4558. doi:10.1002/2016JB013339.
- 935 Jordan, T.E., Isacks, B.L., Allmendinger, R.W., Brewer, J.A.O.N., Ramos, V.A., Ando, C.J., 1983. Andean tectonics
936 related to geometry of subducted Nazca plate. *Geological Society of America Bulletin* 94(3), 341.
937 doi:10.1130/0016-7606(1983)94<341:ATRTGO>2.0.CO;2.
- 938 Kay, S.M., Maksiyev, V., Moscoso, R., Mpodozis, C., Nasi, C., 1987. Probing the evolving Andean Lithosphere:
939 Mid-Late Tertiary magmatism in Chile (29°–30°30'S) over the modern zone of subhorizontal subduction.
940 *Journal of Geophysical Research* 92(B7), 6173. doi:10.1029/JB092iB07p06173.
- 941 Lajoie, K.R., 1986. Coastal tectonics. In: Wallace, R.E. (Ed.), *Active tectonics*. National Academics Press,
942 Washington D.C., pp. 95–124.
- 943 Lamb, S., Davis, P., 2003. Cenozoic climate change as a possible cause for the rise of the Andes. *Nature* 425(6960),
944 792–797. doi:10.1038/nature02049.
- 945 Lohrmann, J., Kukowski, N., Adam, J., Oncken, O., 2003. The impact of analogue material properties on the
946 geometry, kinematics, and dynamics of convergent sand wedges. *Journal of Structural Geology* 25(10), 1691–
947 1711. doi:10.1016/S0191-8141(03)00005-1.
- 948 Lorscheid, T., Rovere, A., 2019. The indicative meaning calculator – quantification of paleo sea-level relationships
949 by using global wave and tide datasets. *Open Geospatial Data, Software and Standards* 4(1), 591.
950 doi:10.1186/s40965-019-0069-8.
- 951 Macharé, J., Ortlieb, L., 1992. Plio-Quaternary vertical motions and the subduction of the Nazca Ridge, central coast
952 of Peru. *Tectonophysics* 205(1-3), 97–108. doi:10.1016/0040-1951(92)90420-B.
- 953 Maldonado, V., Contreras, M., Melnick, D., 2021. A comprehensive database of active and potentially-active
954 continental faults in Chile at 1:25,000 scale. *Scientific data* 8(1), 20. doi:10.1038/s41597-021-00802-4.

955 Manea, V.C., Pérez-Gussinyé, M., Manea, M., 2012. Chilean flat slab subduction controlled by overriding plate
956 thickness and trench rollback. *Geology* 40(1), 35–38. doi:10.1130/G32543.1.

957 Mann, P., Taylor, F.W., Lago, M.B., Quarles, A., Burr, G., 1998. Accelerating late Quaternary uplift of the New
958 Georgia Island Group (Solomon island arc) in response to subduction of the recently active Woodlark spreading
959 center and Coleman seamount. *Tectonophysics* 295(3-4), 259–306. doi:10.1016/S0040-1951(98)00129-2.

960 Marcaillou, B., Collot, J.-Y., Ribodetti, A., d'Acremont, E., Mahamat, A.-A., Alvarado, A., 2016. Seamount
961 subduction at the North-Ecuadorian convergent margin: Effects on structures, inter-seismic coupling and
962 seismogenesis. *Earth and Planetary Science Letters* 433, 146–158. doi:10.1016/j.epsl.2015.10.043.

963 Martinod, J., Regard, V., Letourmy, Y., Henry, H., Hassani, R., Baratchart, S., Carretier, S., 2016a. How do
964 subduction processes contribute to forearc Andean uplift? Insights from numerical models. *Journal of*
965 *Geodynamics* 96, 6–18. doi:10.1016/j.jog.2015.04.001.

966 Martinod, J., Regard, V., Riquelme, R., Aguilar, G., Guillaume, B., Carretier, S., Cortés-Aranda, J., Leanni, L.,
967 Hérail, G., 2016b. Pleistocene uplift, climate and morphological segmentation of the Northern Chile coasts
968 (24°S–32°S): Insights from cosmogenic ¹⁰Be dating of paleoshorelines. *Geomorphology* 274, 78–91.
969 doi:10.1016/j.geomorph.2016.09.010.

970 Melet, A., Teatini, P., Le Cozannet, G., Jamet, C., Conversi, A., Benveniste, J., Almar, R., 2020. Earth Observations
971 for Monitoring Marine Coastal Hazards and Their Drivers. *Surveys in Geophysics* 41(6), 1489–1534.
972 doi:10.1007/s10712-020-09594-5.

973 Melnick, D., 2016. Rise of the central Andean coast by earthquakes straddling the Moho. *Nature Geoscience* 9(5),
974 401–407. doi:10.1038/ngeo2683.

975 Melnick, D., Bookhagen, B., Echtler, H.P., Strecker, M.R., 2006. Coastal deformation and great subduction
976 earthquakes, Isla Santa Maria, Chile (37°S). *Geological Society of America Bulletin* 118(11-12), 1463–1480.
977 doi:10.1130/B25865.1.

978 Melnick, D., Bookhagen, B., Strecker, M.R., Echtler, H.P., 2009. Segmentation of megathrust rupture zones from
979 fore-arc deformation patterns over hundreds to millions of years, Arauco peninsula, Chile. *Journal of*
980 *Geophysical Research: Solid Earth* 114(B1), 6140. doi:10.1029/2008JB005788.

981 Melnick, D., Hillemann, C., Jara-Muñoz, J., Garrett, E., Cortés-Aranda, J., Molina, D., Tassara, A., Strecker, M.R.,
982 2019. Hidden Holocene slip along the coastal El Yolki Fault in Central Chile and its possible link with
983 megathrust earthquakes. *Journal of Geophysical Research: Solid Earth* 124(7), 7280–7302.
984 doi:10.1029/2018JB017188.

985 Melnick, D., Maldonado, V., Contreras, M., 2020. Database of active and potentially-active continental faults in
986 Chile at 1:25,000 scale. PANGAEA - Data Publisher for Earth & Environmental Science.
987 doi:10.1594/PANGAEA.922241.

- 988 Melosh, H.J., Raefsky, A., 1980. The dynamical origin of subduction zone topography. *Geophysical Journal*
989 *International* 60(3), 333–354. doi:10.1111/j.1365-246X.1980.tb04812.x.
- 990 Menant, A., Angiboust, S., Gerya, T., Lacassin, R., Simoes, M., Grandin, R., 2020. Transient stripping of
991 subducting slabs controls periodic forearc uplift. *Nature communications* 11(1), 1823. doi:10.1038/s41467-020-
992 15580-7.
- 993 Morgan, J.K., Bangs, N.L., 2017. Recognizing seamount-forearc collisions at accretionary margins: Insights from
994 discrete numerical simulations. *Geology* 45(7), 635–638. doi:10.1130/G38923.1.
- 995 Müller, R.D., Sdrolias, M., Gaina, C., Roest, W.R., 2008. Age, spreading rates, and spreading asymmetry of the
996 world's ocean crust. *Geochemistry, Geophysics, Geosystems* 9(4). doi:10.1029/2007GC001743.
- 997 Naranjo, J.A., 1987. Interpretacion de la actividad cenozoica superior a lo largo de la Zona de Falla Atacama, Norte
998 de Chile. *Revista Geológica de Chile*(31), 43–55.
- 999 Ortlieb, L., Macharé, J., 1990. Geochronologia y morfoestratigrafia de terrazas marinas del Pleistoceno superior: El
1000 caso de San Juan-Marcona, Peru. *Boletín de la Sociedad Geológica del Perú* 81, 87–106.
- 1001 Ortlieb, L., Zazo, C., Goy, J., Hillaire-Marcel, C., Ghaleb, B., Cournoyer, L., 1996a. Coastal deformation and sea-
1002 level changes in the northern Chile subduction area (23°S) during the last 330 ky. *Quaternary Science Reviews*
1003 15(8-9), 819–831. doi:10.1016/S0277-3791(96)00066-2.
- 1004 Ortlieb, L., Zazo, C., Goy, J.L., Dabrio, C., Macharé, J., 1996b. Pampa del Palo: an anomalous composite marine
1005 terrace on the uprising coast of southern Peru. *Journal of South American Earth Sciences* 9(5-6), 367–379.
1006 doi:10.1016/S0895-9811(96)00020-X.
- 1007 Ota, Y., Miyauchi, T., Paskoff, R., Koba, M., 1995. Plio-Quaternary marine terraces and their deformation along the
1008 Altos de Talinay, North-Central Chile. *Revista Geológica de Chile* 22(1), 89–102.
- 1009 Paris, P.J., Walsh, J.P., Corbett, D.R., 2016. Where the continent ends. *Geophysical Research Letters* 43(23),
1010 12,208-12,216. doi:10.1002/2016GL071130.
- 1011 Pedoja, K., Dumont, J.F., Lamothe, M., Ortlieb, L., Collot, J.-Y., Ghaleb, B., Auclair, M., Alvarez, V., Labrousse,
1012 B., 2006a. Plio-Quaternary uplift of the Manta Peninsula and La Plata Island and the subduction of the Carnegie
1013 Ridge, central coast of Ecuador. *Journal of South American Earth Sciences* 22(1-2), 1–21.
1014 doi:10.1016/j.jsames.2006.08.003.
- 1015 Pedoja, K., Husson, L., Regard, V., Cobbold, P.R., Ostanciaux, E., Johnson, M.E., Kershaw, S., Saillard, M.,
1016 Martinod, J., Furgerot, L., Weill, P., Delcaillau, B., 2011. Relative sea-level fall since the last interglacial stage:
1017 Are coasts uplifting worldwide? *Earth-Science Reviews* 108(1-2), 1–15. doi:10.1016/j.earscirev.2011.05.002.

- 1018 Pedoja, K., Ortlieb, L., Dumont, J.F., Lamothe, M., Ghaleb, B., Auclair, M., Labrousse, B., 2006b. Quaternary
1019 coastal uplift along the Talara Arc (Ecuador, Northern Peru) from new marine terrace data. *Marine Geology*
1020 228(1-4), 73–91. doi:10.1016/j.margeo.2006.01.004.
- 1021 Pilger, R.H., 1981. Plate reconstructions, aseismic ridges, and low-angle subduction beneath the Andes. *Geological*
1022 *Society of America Bulletin* 92(7), 448. doi:10.1130/0016-7606(1981)92<448:PRARAL>2.0.CO;2.
- 1023 Prémaillon, M., Regard, V., Dewez, T.J.B., Auda, Y., 2018. GlobR2C2 (Global Recession Rates of Coastal Cliffs): a
1024 global relational database to investigate coastal rocky cliff erosion rate variations. *Earth Surface Dynamics* 6(3),
1025 651–668. doi:10.5194/esurf-6-651-2018.
- 1026 Rabassa, J., Clapperton, C.M., 1990. Quaternary glaciations of the southern Andes. *Quaternary Science Reviews*
1027 9(2-3), 153–174. doi:10.1016/0277-3791(90)90016-4.
- 1028 Ramos, V.A., Folguera, A., 2009. Andean flat-slab subduction through time. *Geological Society, London, Special*
1029 *Publications* 327(1), 31–54. doi:10.1144/SP327.3.
- 1030 Regard, V., Saillard, M., Martinod, J., Audin, L., Carretier, S., Pedoja, K., Riquelme, R., Paredes, P., Hérail, G.,
1031 2010. Renewed uplift of the Central Andes Forearc revealed by coastal evolution during the Quaternary. *Earth*
1032 *and Planetary Science Letters* 297(1-2), 199–210. doi:10.1016/j.epsl.2010.06.020.
- 1033 Rehak, K., Bookhagen, B., Strecker, M.R., Echtler, H.P., 2010. The topographic imprint of a transient climate
1034 episode: the western Andean flank between 15.5° and 41.5°S. *Earth Surface Processes and Landforms* 35(13),
1035 1516–1534. doi:10.1002/esp.1992.
- 1036 Rodríguez, M.P., Carretier, S., Charrier, R., Saillard, M., Regard, V., Hérail, G., Hall, S., Farber, D., Audin, L.,
1037 2013. Geochronology of pediments and marine terraces in north-central Chile and their implications for
1038 Quaternary uplift in the Western Andes. *Geomorphology* 180-181, 33–46.
1039 doi:10.1016/j.geomorph.2012.09.003.
- 1040 Rohling, E.J., Grant, K., Bolshaw, M., Roberts, A.P., Siddall, M., Hemleben, C., Kucera, M., 2009. Antarctic
1041 temperature and global sea level closely coupled over the past five glacial cycles. *Nature Geoscience* 2(7), 500–
1042 504. doi:10.1038/ngeo557.
- 1043 Rovere, A., Ryan, D., Murray-Wallace, C., Simms, A., Vacchi, M., Dutton, A., Lorscheid, T., Chutcharavan, P.,
1044 Brill, D., Bartz, M., Jankowski, N., Mueller, D., Cohen, K., Gowan, E., 2020. Descriptions of database fields for
1045 the World Atlas of Last Interglacial Shorelines (WALIS). Zenodo. doi:10.5281/ZENODO.3961544.
- 1046 Ruh, J.B., Sallarès, V., Ranero, C.R., Gerya, T., 2016. Crustal deformation dynamics and stress evolution during
1047 seamount subduction: High-resolution 3-D numerical modeling. *Journal of Geophysical Research: Solid Earth*
1048 121(9), 6880–6902. doi:10.1002/2016JB013250.

- 1049 Saillard, M., 2008. Dynamique du soulèvement côtier Pléistocène des Andes centrales Etude de l'évolution
1050 géomorphologique et datations (10Be) de séquences de terrasses marines (Sud Pérou - Nord Chili), Université
1051 Paul Sabatier, Toulouse.
- 1052 Saillard, M., Hall, S.R., Audin, L., Farber, D.L., Hérail, G., Martinod, J., Regard, V., Finkel, R.C., Bondoux, F.,
1053 2009. Non-steady long-term uplift rates and Pleistocene marine terrace development along the Andean margin
1054 of Chile (31°S) inferred from 10Be dating. *Earth and Planetary Science Letters* 277(1-2), 50–63.
1055 doi:10.1016/j.epsl.2008.09.039.
- 1056 Saillard, M., Hall, S.R., Audin, L., Farber, D.L., Regard, V., Hérail, G., 2011. Andean coastal uplift and active
1057 tectonics in southern Peru: 10Be surface exposure dating of differentially uplifted marine terrace sequences (San
1058 Juan de Marcona, ~15.4°S). *Geomorphology* 128(3-4), 178–190. doi:10.1016/j.geomorph.2011.01.004.
- 1059 Santibáñez, I., Cembrano, J., García-Pérez, T., Costa, C., Yáñez, G., Marquardt, C., Arancibia, G., González, G.,
1060 2019. Crustal faults in the Chilean Andes: geological constraints and seismic potential. *Andean Geology* 46(1),
1061 32. doi:10.5027/andgeoV46n1-3067.
- 1062 Scholl, D.W., Huene, R. von, 2007. Crustal recycling at modern subduction zones applied to the past—Issues of
1063 growth and preservation of continental basement crust, mantle geochemistry, and supercontinent reconstruction.
1064 In: 4-D Framework of Continental Crust. Geological Society of America, pp. 9–32.
- 1065 Schwanghart, W., Kuhn, N.J., 2010. TopoToolbox: A set of Matlab functions for topographic analysis.
1066 *Environmental Modelling & Software* 25(6), 770–781. doi:10.1016/j.envsoft.2009.12.002.
- 1067 Schweller, W.J., Kulm, L.D., Prince, R.A., 1981. Tectonics, structure, and sedimentary framework of the Peru-Chile
1068 Trench. *Geological Society of America Memoir* 154, 323–350. doi:10.1130/MEM154-p323.
- 1069 Shackleton, N.J., Sánchez-Goñi, M.F., Paillet, D., Lancelot, Y., 2003. Marine Isotope Substage 5e and the Eemian
1070 Interglacial. *Global and Planetary Change* 36(3), 151–155. doi:10.1016/S0921-8181(02)00181-9.
- 1071 Shepherd, A., Wingham, D., 2007. Recent sea-level contributions of the Antarctic and Greenland ice sheets. *Science*
1072 (New York, N.Y.) 315(5818), 1529–1532. doi:10.1126/science.1136776.
- 1073 Siddall, M., Chappell, J., Potter, E.-K., 2006. Eustatic sea level during past interglacials. In: Sirocko, F., Litt, T.,
1074 Claussen, M., Sanchez-Goni, M.-F. (Eds.), *The climate of past interglacials*. Elsevier, Amsterdam, pp. 75–92.
- 1075 Sobolev, S.V., Babeyko, A.Y., 2005. What drives orogeny in the Andes? *Geology* 33(8), 617–620.
1076 doi:10.1130/G21557AR.1.
- 1077 Stern, C.R., 1991. Role of subduction erosion in the generation of Andean magmas. *Geology* 19(1), 78.
1078 doi:10.1130/0091-7613(1991)019<0078:ROSEIT>2.3.CO;2.
- 1079 Stewart, I.S., Sauber, J., Rose, J., 2000. Glacio-seismotectonics: ice sheets, crustal deformation and seismicity.
1080 *Quaternary Science Reviews* 19(14-15), 1367–1389. doi:10.1016/S0277-3791(00)00094-9.

- 1081 Stirling, C.H., Esat, T.M., Lambeck, K., McCulloch, M.T., 1998. Timing and duration of the Last Interglacial:
1082 evidence for a restricted interval of widespread coral reef growth. *Earth and Planetary Science Letters* 160(3-4),
1083 745–762. doi:10.1016/S0012-821X(98)00125-3.
- 1084 Strecker, M.R., Alonso, R.N., Bookhagen, B., Carrapa, B., Hilley, G.E., Sobel, E.R., Trauth, M.H., 2007. Tectonics
1085 and Climate of the Southern Central Andes. *Annual Review of Earth and Planetary Sciences* 35(1), 747–787.
1086 doi:10.1146/annurev.earth.35.031306.140158.
- 1087 Suárez, G., Molnar, P., Burchfiel, B.C., 1983. Seismicity, fault plane solutions, depth of faulting, and active
1088 tectonics of the Andes of Peru, Ecuador, and southern Colombia. *Journal of Geophysical Research* 88(B12),
1089 10403–10428. doi:10.1029/JB088iB12p10403.
- 1090 Taylor, F.W., Frohlich, C., Lecolle, J., Strecker, M., 1987. Analysis of partially emerged corals and reef terraces in
1091 the central Vanuatu Arc: Comparison of contemporary coseismic and nonseismic with quaternary vertical
1092 movements. *Journal of Geophysical Research* 92(B6), 4905. doi:10.1029/JB092iB06p04905.
- 1093 Trenhaile, A.S., 2002. Modeling the development of marine terraces on tectonically mobile rock coasts. *Marine*
1094 *Geology* 185(3-4), 341–361. doi:10.1016/S0025-3227(02)00187-1.
- 1095 Turcotte, D.L., Schubert, G., 1982. *Geodynamics: Applications of Continuum Physics to Geological Problems*. John
1096 Wiley, New York (450 pp.).
- 1097 Veloza, G., Styron, R., Taylor, M., Mora, A., 2012. Open-source archive of active faults for northwest South
1098 America. *GSA Today* 22(10), 4–10. doi:10.1130/GSAT-G156A.1.
- 1099 Venzke, E., 2013. *Volcanoes of the World*, v. 4.3.4. Global Volcanism Program.
- 1100 Victor, P., Sobiesiak, M., Glodny, J., Nielsen, S.N., Oncken, O., 2011. Long-term persistence of subduction
1101 earthquake segment boundaries: Evidence from Mejillones Peninsula, northern Chile. *Journal of Geophysical*
1102 *Research* 116(B2), 93. doi:10.1029/2010JB007771.
- 1103 Villegas-Lanza, J.C., Chlieh, M., Cavalié, O., Tavera, H., Baby, P., Chire-Chira, J., Nocquet, J.-M., 2016. Active
1104 tectonics of Peru: Heterogeneous interseismic coupling along the Nazca megathrust, rigid motion of the
1105 Peruvian Sliver, and Subandean shortening accommodation. *Journal of Geophysical Research: Solid Earth*
1106 121(10), 7371–7394. doi:10.1002/2016JB013080.
- 1107 von Huene, R., Corvalán, J., Flueh, E.R., Hinz, K., Korstgard, J., Ranero, C.R., Weinrebe, W., 1997. Tectonic
1108 control of the subducting Juan Fernández Ridge on the Andean margin near Valparaiso, Chile. *Tectonics* 16(3),
1109 474–488. doi:10.1029/96TC03703.
- 1110 von Huene, R., Scholl, D.W., 1991. Observations at convergent margins concerning sediment subduction,
1111 subduction erosion, and the growth of continental crust. *Geology* 29(3), 279. doi:10.1029/91RG00969.

- 1112 Wang, K., Bilek, S.L., 2011. Do subducting seamounts generate or stop large earthquakes? *Geology* 39(9), 819–822.
1113 doi:10.1130/G31856.1.
- 1114 Wang, K., Bilek, S.L., 2014. Invited review paper: Fault creep caused by subduction of rough seafloor relief.
1115 *Tectonophysics* 610, 1–24. doi:10.1016/j.tecto.2013.11.024.
- 1116 Watts, A.B., Daly, S.F., 1981. Long Wavelength Gravity and Topography Anomalies. *Annual Review of Earth and*
1117 *Planetary Sciences* 9, 415–448.